The Astrophysical Journal, 681:1099–1115, 2008 July 10

THE MULTIWAVELENGTH SURVEY BY YALE-CHILE (MUSYC): WIDE *K*-BAND IMAGING, PHOTOMETRIC CATALOGS, CLUSTERING, AND PHYSICAL PROPERTIES OF GALAXIES AT $z \sim 2$

Guillermo A. Blanc,[1,2] Paulina Lira,[1] L. Felipe Barrientos,[3] Paula Aguirre,[3] Harold Francke,[1] Edward N. Taylor,[4] Ryan Quadri,[5] Danilo Marchesini,[5] Leopoldo Infante,[3] Eric Gawiser,[6] Patrick B. Hall,[7] Jon P. Willis,[8] David Herrera,[9] and José Maza[1] (for the MUSYC Collaboration)

Received 2008 January 7; accepted 2008 March 5

ABSTRACT

We present *K*-band imaging of two $\sim 30' \times 30'$ fields covered by the Multiwavelength Survey by Yale-Chile (MUSYC) Wide NIR Survey. The SDSS 1030+05 and Cast 1255 fields were imaged with the Infrared Side Port Imager (ISPI) on the 4 m Blanco telescope at the Cerro Tololo Inter-American Observatory (CTIO) to a 5 σ point-source limiting depth of $K \sim 20$ (Vega). Combining these data with the MUSYC optical *UBVRIz* imaging, we created multiband *K*-selected source catalogs for both fields. These catalogs, together with the MUSYC *K*-band catalog of the Extended Chandra Deep Field South (ECDF-S) field, were used to select $K < 20$ *BzK* galaxies over an area of 0.71 deg^2. This is the largest area ever surveyed for *BzK* galaxies. We present number counts, redshift distributions, and stellar masses for our sample of 3261 *BzK* galaxies (2502 star-forming [*sBzK*] and 759 passively evolving [*pBzK*]), as well as reddening and star formation rate estimates for the star-forming *BzK* systems. We also present two-point angular correlation functions and spatial correlation lengths for both *sBzK* and *pBzK* galaxies and show that previous estimates of the correlation function of these galaxies were affected by cosmic variance due to the small areas surveyed. We have measured correlation lengths r_0 of 8.89 ± 2.03 and 10.82 ± 1.72 Mpc for *sBzK* and *pBzK* galaxies, respectively. This is the first reported measurement of the spatial correlation function of passive *BzK* galaxies. In the ΛCDM scenario of galaxy formation, these correlation lengths at $z \sim 2$ translate into minimum masses of $\sim 4 \times 10^{12}$ and $\sim 9 \times 10^{12}\ M_\odot$ for the dark matter halos hosting *sBzK* and *pBzK* galaxies, respectively. The clustering properties of the galaxies in our sample are consistent with their being the descendants of bright Lyman break galaxies at $z \sim 3$, and the progenitors of present-day $>1L^*$ galaxies.

Subject headings: catalogs — galaxies: evolution — galaxies: high-redshift — galaxies: statistics — large-scale structure of universe — surveys

1. INTRODUCTION

The processes involved in the formation of galaxies and the phenomena that drive their consequent evolution are among the most important and fundamental problems in astronomy. In order to understand these processes, we need to study the properties of statistically significant samples of galaxies throughout cosmic time. During the last decade, there have been enormous advances in this direction. The advent of 8 m class telescopes, a new generation of wide-field optical imagers and infrared detectors, and a series of different photometric selection techniques have provided us with the ability to select large samples of intermediate- and high-redshift galaxies. Probably the most successful method applied to date for building these samples has been the Lyman-break galaxy (LBG) dropout technique at $z \sim 3$ (Steidel et al. 1996), which has recently been extended to lower redshifts ($z \sim 2$) using $U_n G\mathcal{R}$ two-color photometry for the BM/BX galaxy selection (Erb et al. 2003; Adelberger et al. 2004). Other types of $z > 1$ galaxies include narrowband-selected Lyα emitters (LAEs; e.g., Hu et al. 1998; Gawiser et al. 2006b; Gronwall et al. 2007), distant red galaxies (DRGs) selected by their red near-infrared colors $J - K > 2.3$ (Franx et al. 2003; van Dokkum et al. 2003), extremely red objects (EROs) selected by their red optical to near-infrared colors, usually $R - K > 5$ (Thompson et al. 1999; Cimatti et al. 2002a), as well as far-IR and submillimeter-detected, highly obscured galaxies at high redshift (Smail et al. 2000).

Another selection technique of great importance to this work was introduced by Daddi et al. (2004), who defined two-color criteria based on *BzK* photometry of *K*-selected galaxies that are capable of identifying both passive (*pBzK*) and star-forming (*sBzK*) galaxies in the $1.4 < z < 2.5$ range, and of distinguishing between the two populations. Among the available NIR bands, the *K* band is the best choice for detecting intermediate- and high-redshift galaxies from the ground. It is the reddest band for which sensitivities and angular resolutions comparable to the ones obtained by ground-based optical imaging can be achieved. Since galaxies can be efficiently selected by the fact that their rest-frame optical emission is redshifted to the NIR bands, *K*-selection gives us access to the "spectroscopic redshift desert" ($1.4 < z < 2$), where galaxies show no distinctive spectral features in their observed optical spectra. One of the main advantages of the *BzK* technique is that it is almost insensitive to the amount of reddening in the star-forming galaxies. NIR observations allow us to detect and identify distant galaxies in a more unbiased way than optical imaging, since the effects of dust extinction are lower

[1] Departamento de Astronomía, Universidad de Chile, Santiago, Chile; gblancm@astro.as.utexas.edu.
[2] Astronomy Department, University of Texas, Austin, TX.
[3] Departamento de Astronomía, Pontificia Universidad Católica de Chile, Santiago, Chile.
[4] Leiden Observatory, Leiden University, Leiden, Netherlands.
[5] Astronomy Department, Yale University, New Haven, CT.
[6] Department of Physics and Astronomy, Rutgers University, Piscataway, NJ.
[7] Department of Physics and Astronomy, York University, Toronto, ON, Canada.
[8] Department of Physics and Astronomy, University of Victoria, Victoria, BC, Canada.
[9] National Optical Astronomy Observatory, Tucson, AZ.

at these wavelengths, and the observed light is dominated by evolved stellar populations, making detection more independent of spectral type. NIR luminosity is directly related to the stellar mass of the galaxy. The *BzK* selection technique provides us with a powerful tool to explore the $z \sim 2$ universe in a relatively unbiased way.

Despite all these advances and the fact that we have converged into a single cosmological model, the assembling and evolution of galaxies remains poorly understood. We still lack a comprehensive picture of galaxy populations at intermediate and high redshifts. All the selection techniques mentioned above only give partial views of the universe at specific epochs, and the biases involved in their selection, as well as the overlapping between different techniques, is just starting to be understood (Reddy et al. 2005; van Dokkum et al. 2006; Quadri et al. 2007b; Lane et al. 2007; Grazian et al. 2007). In particular, optically selected samples require galaxies to be bright in their rest-frame UV, and are therefore biased against obscured systems in which the UV luminosity of a star-forming galaxy is quenched by the dust content of its interstellar medium (ISM), as well as against passively evolving systems with little intrinsic UV emission. Hence, studies based on these samples constrain the behavior and evolution of unobscured star formation activity more than the actual stellar mass assembly of these systems. At $z \sim 2$, the most popular selection techniques used so far include UV-selected BM/BX galaxies, DRGs, and *BzK* galaxies. Reddy et al. (2005) showed that BM/BX selection misses 40% of star-forming *BzK* galaxies when both samples are subject to a common NIR magnitude limit of $K < 20$. Recent work by Quadri et al. (2007b) estimated a larger missing fraction of 60% to $K < 20$, which decreases to 35% when going to deeper NIR fluxes ($K < 21$). Grazian et al. (2007) computed an even larger fraction of missed *sBzK* galaxies of 62% at a deeper NIR magnitude limit of $K < 22$. In all the mentioned works, BM/BX galaxies completely miss passive *BzK* galaxies at $z \sim 2$. UV-based selection techniques perform even more poorly when trying to recover the DRG population. Quadri et al. (2007b) showed that only 32% of DRGs in the $K < 21$ MUSYC Deep NIR sample have colors consistent with the BM/BX/LBG criteria, and only 14% also fulfill the $\mathcal{R}_{\rm AB} < 25.5$ cut used in most ground-based optically selected samples. This is in agreement with the 12% recovery fraction estimated by Reddy et al. (2005) to the same NIR magnitude limit, and higher than the 3% fraction computed by Grazian et al. (2007) for a deeper $K < 22$ DRG sample.

On the other hand, the *sBzK* criteria successfully recover 80% of the $z > 1.4$, $K < 20$ BM/BX galaxies in Reddy's (2005) sample, in agreement with the results of Quadri et al. (2007b) for a $K < 21$ sample. This fraction improves to up to 99% when going to a fainter NIR limit of $K < 22$ (Grazian et al. 2007). The *BzK* technique is also much better than rest-frame UV selection techniques at recovering the DRG population. For a bright $K < 19.3$ sample of DRGs, Lane et al. (2007) obtained a recovery fraction of 55% that were selected as either *sBzK* or *pBzK*. A higher fraction of 65% was obtained by Reddy et al. (2005) for $K < 21$ DRGs, again in agreement with the results of Quadri et al. (2007b). When going to fainter NIR fluxes ($K < 22$), Grazian et al. (2007) estimated an almost complete recovery fraction of 99%. These numbers show that the *BzK* technique is the most inclusive galaxy selection method at $z \sim 2$, mostly because it is able to include galaxies that span a wide range of both optical and optical-to-NIR colors.

Previous samples of *BzK* galaxies include the seminal work by Daddi et al. (2004), who selected $K < 20$ *BzK* galaxies over an area of 52 arcmin^2, a survey by Kong et al. (2006), who covered 320 arcmin^2 to $K < 20$ and 920 arcmin^2 to a shallower depth of $K = 19$, and more recent work by Lane et al. (2007), who surveyed 0.56 deg^2 to $K = 20.6$ in the UKIDSS field, and Hayashi et al. (2007), who selected very faint *BzK* galaxies ($K = 21.3$) over a 180 arcmin^2 area in the Subaru Deep Field.

In this work, we present the MUSYC Wide NIR Survey and the clustering and physical properties of *BzK* galaxies selected over an area of 0.71 deg^2 to a limiting depth of $K = 20$. This is the largest area ever surveyed for *BzK* galaxies and the largest sample of these objects available to this depth. In § 2, we introduce the MUSYC survey and present the Wide NIR Survey design. Sections 3 and 4 discuss the observations and data reduction. Source detection, photometry, and the procedures used to build the *K*-selected source catalogs are discussed in § 5. In § 6, we explain our star-galaxy classification method, and we present *K*-band-selected galaxy number counts in § 7. We present the details of the *BzK* selection technique used in this paper in § 8. The results from the analysis of the selected *BzK* sample, redshift distributions, physical properties, and clustering are presented in § 9. Finally, we summarize our results and present conclusions in § 10.

All optical magnitudes are given in the AB system, and NIR magnitudes in the Vega system. Throughout the paper, we have adopted the standard cosmological parameters, $H_0 = 71$ km s^{-1} Mpc^{-1}, $\Omega_M = 0.27$, $\Omega_\Lambda = 0.73$, and $\sigma_8 = 0.8$. All quantities reported are comoving, so correlation lengths scale as h_{70}^{-1}, number densities as h_{70}^{3}, and halo masses as h_{70}^{-1} unless explicitly stated.

2. THE MUSYC WIDE NIR SURVEY

The Multiwavelength Survey by Yale-Chile (MUSYC) consists of deep optical (*UBVRIz*) and near-infrared imaging of four $30' \times 30'$ fields. The survey design and optical images are described by Gawiser et al. (2006a). The four fields (Extended Hubble Deep Field South [EHDF-S], Extended Chandra Deep Field South [ECDF-S], SDSS 1030+05, and Cast 1255) are at high Galactic latitudes ($|b| > 30$) and show low 100 μm emission and $N_{\rm H}$ in order to minimize contamination by stars and the Galaxy ISM.

The near-infrared imaging of the MUSYC fields forms part of two complementary campaigns. The MUSYC Deep NIR Survey imaged four $10' \times 10'$ subfields in three NIR bands to typical 5 σ limiting depths of $J \sim 22.5$, $H \sim 21.5$, and $K \sim 21$. The survey design and results were presented by Quadri et al. (2007b). The MUSYC Wide NIR Survey consists of *K*-band imaging of three full $30' \times 30'$ MUSYC fields (ECDS-S, SDSS 1030+05, and Cast 1255) to a limiting depth of $K \sim 20$, as well as *J*- and *H*-band imaging of the ECDF-S.

In this work, we present the NIR imaging and *K*-band-selected source catalogs for two fields of the Wide NIR Survey: SDSS 1030+05 and Cast 1255 (hereafter 1030 and 1255). Table 1 gives relevant information about the surveyed fields. The wide NIR imaging of the ECDF-S will be presented by E. Taylor et al. (2008, in preparation). *H*-band imaging to a depth similar to that of EHDF-S is already available from the Las Campanas Infrared Survey (Chen et al. 2002).

MUSYC also includes narrowband 5000 Å imaging of the whole square degree to enable searches for Lyα emitters and Lyα blobs at $z = 3.1$ (Gawiser et al. 2006b; G. A. Blanc et al. 2008, in preparation), mid-infrared from the *Spitzer* IRAC MUSYC Public Legacy Survey (SIMPLE; I. Labbé et al. 2008, in preparation), *Chandra* X-ray imaging (Virani et al. 2006) of the ECDF-S, *XMM-Newton* X-ray observations of 1030, and spectroscopic follow-up of the four fields (P. Lira et al. 2008, in preparation).

TABLE 1
MUSYC WIDE NIR FIELDS

Field	R.A. (J2000.0)	Decl. (J2000.0)	$E(B-V)$[a] (mag)
SDSS 1030+05	10 30 27.1	05 24 55	0.02
Cast 1255	12 55 40.0	01 07 00	0.02
E-CDFS.....	03 32 29.0	−27 48 47	0.01

NOTE.—Units of right ascension are hours, minutes, and seconds, and units of declination are degrees, arcminutes, and arcseconds.
[a] From Schlegel et al. (1998).

More information about MUSYC, together with publicly available data, can be found online.[10]

3. OBSERVATIONS

Our *K*-band images of the 1030 and 1255 fields were taken on the nights of 2003 January 31, 2003 May 7–12, 2004 February 11–14, 2004 April 10–13, 2005 April 14–22, and 2006 April 18–23 using the Infrared Side Port Imager (ISPI) on the 4 m Blanco Telescope at the Cerro Tololo Inter-American Observatory (CTIO). The detector is a 2K × 2K HgCdTe HAWAII-2 array that delivers images with a 0.305″ pixel^{-1} scale over a field of view (FOV) of 10.5′ × 10.5′. Since the FOV of ISPI is smaller than the 30′ × 30′ area covered by MUSYC optical images, we divided each field into nine subfields (NE, E, SE, S, SW, W, NW, N, C), which we later mosaic as described in § 4.4.

The dominance of the sky background and its rapid variability determines the observing strategy in the *K* band. Dithered short exposures are necessary in order to subtract the background and keep the number of counts within the linear regime of the detector. Individual raw frames are the result of coadding short exposures. Our science frames have integration times of 4 × 15, 5 × 12, or 6 × 10 s, depending on the intensity of the sky background at the moment of the observations. We used a quasi-random dither pattern inside a 45″ box.

Dome flats and dark frames were obtained at the beginning and the end of every night. Flats are built by taking the difference between the combined flat frames taken with the lamp on and the combined frames taken with the lamp off in order to subtract the thermal background.

The K' filter on ISPI was replaced in 2004 April by a new K_s filter. Around 20% of our observations were completed using the K' filter, and the rest of the survey was completed using the new K_s filter. Figure 1 shows the transmission curves of the two filters after multiplying by the detector quantum efficiency and the atmospheric transmission at CTIO. The difference in effective wavelength between the two filters is ∼30 Å, which is negligible compared to the filters' width. Quadri et al. (2007b) calculated a conversion between the filters of 0.02 mag, which is smaller than our typical photometric uncertainties. Therefore, in the following discussion we do not distinguish between the two filters, and we simply refer to them as the *K* filter.

4. DATA REDUCTION AND IMAGE PROPERTIES

4.1. *Image Processing*

Data reduction was performed using standard IRAF[11] routines, modified IRAF routines, and custom IDL tasks. Our reduction scheme is based on the methods described by Labbé et al. (2003) and Quadri et al. (2007b). The external IRAF package XDIMSUM[12] was used throughout most of the steps of the reduction.

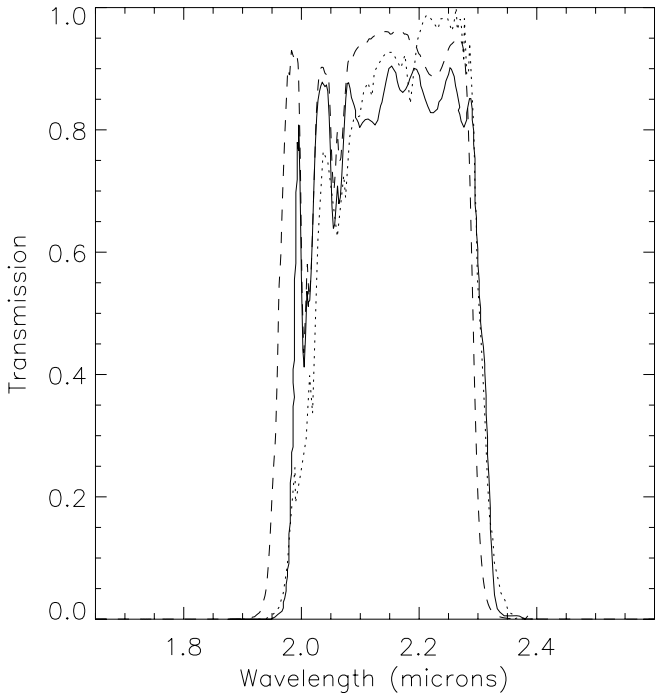

FIG. 1.—Transmission curves of the K' (*dashed line*) and the K_s (*solid line*) filters after multiplying by the detector's quantum efficiency and the atmospheric transmission. The transmission for the K_s 2MASS filter (*dotted line*) is also shown.

We subtracted dark frames of the same exposure time and number of coadds from our science images. Flat frames were constructed for each night as described above, but flat-fielding was not performed until after background subtraction. This approach was adopted because the multiplicative nature of the flat-fielding process scales up the contribution to the noise coming from the uncertainty in the flat frame by the number of counts in the science image (Joyce 1992). This can be shown by deriving the uncertainty in a given pixel after background subtraction and flat-fielding. We consider the two cases where (1) background subtraction is performed before flat-fielding and (2) flat-fielding is performed before background subtraction.

Consider a pixel p with background flux b and object flux o in the image under construction, but only background flux in the other N frames used to estimate the background. In case (1), the value of the pixel after background subtraction is

$$p = b + o - \langle b \rangle, \tag{1}$$

and the uncertainty is

$$\sigma_p^2 = \sigma_b^2 + \sigma_o^2 + \sigma_b^2/N. \tag{2}$$

Now we divide by the flat, and we get

$$p = \frac{b + o - \langle b \rangle}{f}, \tag{3}$$

[10] See http://www.astro.yale.edu/musyc/.
[11] IRAF is distributed by the National Optical Astronomy Observatories, which are operated by the Association of Universities for Research in Astronomy, Inc., under cooperative agreement of the National Science Foundation.
[12] XDIMSUM is the Experimental Deep Infrared Mosaicking Software package developed by L. Davis, and it is available at http://iraf.noao.edu/iraf/ftp/iraf/extern/xdimsum.

and the final uncertainty in case (1) becomes

$$\sigma^2_{p,1} = \frac{\sigma_b^2 + \sigma_o^2 + \sigma_b^2/N}{f^2} + \frac{(b+o)^2\sigma_f^2}{f^4} - \frac{2(b+o)\langle b\rangle\sigma_f^2}{f^4} + \frac{\langle b\rangle^2\sigma_f^2}{f^4}. \quad (4)$$

Now, in case (2) we first divide by the flat, obtaining

$$p = \frac{b+o}{f}, \quad (5)$$

with an uncertainty

$$\sigma_p^2 = \frac{\sigma_b^2 + \sigma_o^2}{f^2} + \frac{(b+o)^2\sigma_f^2}{f^4}, \quad (6)$$

and then subtract the background, obtaining

$$p = \frac{(b+o)}{f} - \frac{\langle b\rangle}{f}, \quad (7)$$

with a final uncertainty for case (2) of

$$\sigma^2_{p,2} = \frac{\sigma_b^2 + \sigma_o^2}{f^2} + \frac{(b+o)^2\sigma_f^2}{f^4} + \frac{\sigma_b^2}{Nf^2} + \frac{\langle b\rangle^2\sigma_f^2}{f^4}. \quad (8)$$

It can be seen that the noise in case (2) is higher than in case (1) by $2(b+o)\langle b\rangle\sigma_f^2/f^4$. Since the typical background level in our images is $b \sim 30{,}000$ counts, and after sky subtraction $\sim$0 counts, it is clear that the contribution from the uncertainty in the flat frame will be strongly suppressed by flat-fielding after sky subtraction. In the above derivation, we have neglected the contributions of dark current and read noise.

Background subtraction was performed using a two-phase process that avoids overestimating the background around bright objects. A background image is created for every science frame by combining eight dithered frames adjacent in time. The combination is an average excluding the lowest and highest value at every pixel position. These background frames are subtracted from the science images to create preliminary background-subtracted images. The positions of six stars are used to calculate the relative offsets between dithered background-subtracted frames, and the images are then combined after registering them to a common reference using fractional pixel shifts.

Objects are then detected in the combined image using a thresholding algorithm, and an object mask is created. The mask is deregistered to the reference of each original dithered science frame, and the background subtraction process is repeated. In this second phase, the background image for each science frame is created as above, but with masking added to the detected objects in the time-adjacent frames before combining them. This background frame is then subtracted from the science image.

A second set of stars in these final sky-subtracted images is used to measure the FWHM and calculate the relative flux scale between the images. The central 300×300 pixel region of each frame is used to calculate the pixel-to-pixel rms of the background. These values are used to compute weights used to optimize the signal-to-noise ratio (S/N) in the seeing disk during the combination of the background-subtracted images. The weights are given by

$$w_i = \frac{1}{(\text{flux scale}_i \times \text{rms}_i \times \text{FWHM}_i)^2}. \quad (9)$$

TABLE 2
1030 and 1255 Subfields *K*-Band Image Properties

Field	Subfield	Zero Point (mag)	FWHM[a] (arcsec)	5 σ Depth[b] (mag)
SDSS 1030+05	C	21.48 ± 0.02	0.9	20.22
	NE	22.01 ± 0.02	0.9	19.87
	E	21.99 ± 0.02	0.9	19.87
	SE	22.14 ± 0.03	0.9	20.00
	S	21.94 ± 0.03	0.9	19.69
	SW	22.02 ± 0.02	1.0	19.73
	W	22.05 ± 0.02	1.1	19.92
	NW	21.98 ± 0.02	1.0	19.68
	N	22.03 ± 0.02	1.1	19.72
Cast 1255	C	21.94 ± 0.02	0.9	19.86
	NE	22.44 ± 0.03	0.9	19.84
	E	22.25 ± 0.03	1.0	19.72
	SE	22.38 ± 0.01	0.9	20.00
	S	22.40 ± 0.03	0.9	19.77
	SW	22.20 ± 0.03	1.0	19.77
	W	22.27 ± 0.03	0.9	19.89
	NW	22.40 ± 0.02	0.9	20.04
	N	22.28 ± 0.02	1.0	20.03

[a] Before PSF matching.
[b] Vega magnitudes, after PSF matching.

A bad pixel mask (BPM) is created by flagging all 4 σ deviant pixels in the flat. XDIMSUM uses a cosmic-ray detection algorithm and combines this information with the BPM to create a rejection mask for each science frame. Satellite trails found during the visual inspection of the images are added by hand to the corresponding rejection mask. The ISPI detector is not able to properly flush extremely bright pixels during readout, as it retains memory of previous exposures in the cores of bright objects. To avoid residuals from previous exposures, we construct a previous-frame bright-object mask for each science image.

All background-subtracted frames are visually inspected in order to reject bad-quality images. There are two main reasons for rejection. The first is catastrophic background subtraction on images due to extreme variations of the background. The second is that the point-spread function (PSF) has a poor shape due to focusing and tracking problems. Around 10% of our images were rejected because of these problems. All the accepted background-subtracted images are then flat-fielded, dividing by the normalized dome flat.

Flat-fielded images usually show residuals caused by variability of the bias structure of ISPI's detector. We remove these features by fitting a low-order polynomial surface to each quadrant of the images after masking the objects and subtracting this surface from the images. Finally, all the images are registered and combined using the above weights, rejecting bad pixels, cosmic rays, and residuals from previous frames. An exposure time map is also generated. Details about the *K*-band images obtained for each subfield in 1030 and 1255 are given in Table 2.

4.2. *Astrometric Projection, PSF Matching, and Photometric Calibration*

In order to measure accurate colors, we need to perform aperture photometry in different bands over the same physical region

TABLE 3
MUSYC Optical Images of 1030 and 1255

Field	Filter	Zero Point (mag)	FWHM[a] (arcsec)	5 σ Depth[b] (mag)
SDSS 1030+05	*U*	22.06	1.1	25.56
	B	24.97	1.0	25.91
	V	25.48	0.9	25.90
	R	25.75	0.9	25.81
	I	25.36	0.9	25.00
	z	24.36	1.0	23.75
Cast 1255	*U*	23.32	1.2	25.62
	B	24.84	1.3	25.53
	V	24.90	1.1	25.42
	R	25.66	1.2	25.08
	I	24.94	1.1	24.00
	z	24.30	1.0	22.81

[a] Before PSF matching.
[b] AB magnitudes, after PSF matching.

as that projected on the sky. The MUSYC optical images have been resampled to a tangent plane projection with a uniform pixel scale and show an rms astrometric error of 0.2″ (Gawiser et al. 2006a). We reprojected the *K*-band images so that they share the same projection, image size, and world coordinate system as the optical images.

We used the standard IRAF tasks GEOMAP and GEOTRAN to compute and apply a transformation between the logical coordinate system of the ISPI images and the logical system of the reference MUSYC *BVR* image. For each subfield image, we used the positions of ~100 stars detected in both the *K*-band and the *BVR* image to fit the coefficients of the two-dimensional sixth order Chebyshev polynomials used for the transformation. The coordinates of the stars in the transformed *K*-band images show an average rms of 0.05″ with respect to the coordinates in the *BVR* image, so our astrometric error is dominated by the uncertainty in the optical images. After resampling, the pixel scale changes from 0.305″ pixel^{-1} to 0.267″ pixel^{-1}.

The measurement of accurate colors requires matching the PSF of the optical and *K*-band images. We built an empirical PSF for each *K*-band subfield image by registering and combining the images of ~40 stars. We used the same method with ~120 stars to build empirical PSFs for the optical images in each band for the two fields. Tables 2 and 3 present the FWHMs of the empirical PSFs of the *K*-band and optical images, respectively. Since the PSF shows broader wings than a Gaussian profile of the same FWHM, convolution with a purely Gaussian kernel is not able to match both the core and the wings of the PSF at the same time. This implies the need to use a non-Gaussian kernel to obtain accurate PSF matching. We matched the PSFs of all the images to a Moffat profile with a FWHM of 1.2″ for 1030 and 1.3″ for 1255. These target PSFs were chosen to be slightly broader (in both the core and the wings) than the PSF of the image with the largest FWHM in the field.

We used the IRAF task LUCY to compute the appropriate convolution kernels for the PSF matching using the Lucy-Richardson iterative algorithm (Richardson 1972; Lucy 1974). LUCY deconvolves the target PSF into the input PSF and a convolution kernel. The kernels are then normalized and convolved with the images to match their PSFs to the target Moffat profile. In order to quantify the quality of the method, we constructed growth curves for all the stars used to build the empirical PSF, and median-combined them to create a master growth curve for each PSF-matched image. After convolution, the master growth curve matches the Moffat profile growth curve to better than 1% at all radii for all the images.

We flux-calibrated our images using the 2MASS survey (Skrutskie et al. 2006). As can be seen in Figure 1, the 2MASS *K* band is very similar to the ISPI *K* band used in this work. We have computed and applied a correction of 0.03 mag to the zero points to account for the difference in the filters, which is on the order of our photometric errors. In each of our *K*-band subfields, we performed photometry in a 14″ diameter aperture on an average of 20 stars that have 2MASS counterparts and that are not affected by saturation, nonlinearity, or close neighbors in the MUSYC imaging. We calculated the zero points of each subfield image by comparing our 14″ aperture magnitudes to the aperture-corrected *K*-band magnitudes of the same stars in the 2MASS point-source catalog (which were measured in 4″ apertures and corrected using a curve of growth measured out to 14″). Uncertainties in the zero points were computed based on the deviation of the zero-point values obtained for single stars and are typically ~0.02 mag. Table 2 presents the zero-point values for each subfield in 1030 and 1255. All subfields were scaled to the zero point with the lowest uncertainty in the field, so the zero points of our final *K*-band images are 22.03 for the 1030 field and 22.38 for the 1255.

4.3. *Correlated Noise Properties*

Derivations of photometric uncertainties typically assume that the background noise properties are characterized by Poisson statistics, so that the background noise in a given aperture is simply given by $(n_{\rm pix})^{1/2}\sigma_{\rm pix}$, where $\sigma_{\rm pix}$ is the pixel-to-pixel rms, and $n_{\rm pix}$ is the number of pixels in the aperture. This assumption is only valid when the pixels are uncorrelated and can be treated as independent experiments. Subpixel shifts used to register the images, astrometric reprojection, and PSF matching introduce correlations between pixels. Previous work has shown that assuming Poisson statistics in the presence of correlated pixels significantly underestimates the uncertainties in the background (Labbé et al. 2003; Gawiser et al. 2006a; Quadri et al. 2007b). Proper characterization of the noise properties of our images is of great importance, since the quality of χ^2 fits during photometric redshift estimations relies on the photometric uncertainties.

We use the "empty aperture" method (Labbé et al. 2003) to empirically determine the noise properties of our NIR subfields and optical images. Briefly, we randomly place a large number (5000) of apertures of area $n_{\rm pix}$ on our images, reject all apertures falling on sources, and measure the flux in the remaining ones. A histogram of the measured fluxes is constructed, and we perform a Gaussian fit to it. The rms of the background in an aperture of area $n_{\rm pix}$ is given by the σ of the Gaussian fit. We repeat the process six times for each image and take the average σ. The method is illustrated by Figure 2, which shows the histogram of enclosed fluxes for apertures of two different sizes. It is clear that the background noise is well described by a Gaussian distribution. Tables 2 and 3 give the 5 σ point-source limiting depth of our images for an aperture size of 1.4 × FWHM (see § 5.2).

We used the same method to measure the dependence of noise on aperture size in the final *K*-band mosaics (built as explained in § 4.4). We measured the rms on a series of increasing apertures with diameters between 0.5″ and 4.0″ (see Fig. 3) and fitted the dependence using the following parameterization:

$$\sigma_n = \alpha\sigma_1 n_{\rm pix}^{\beta}, \tag{10}$$

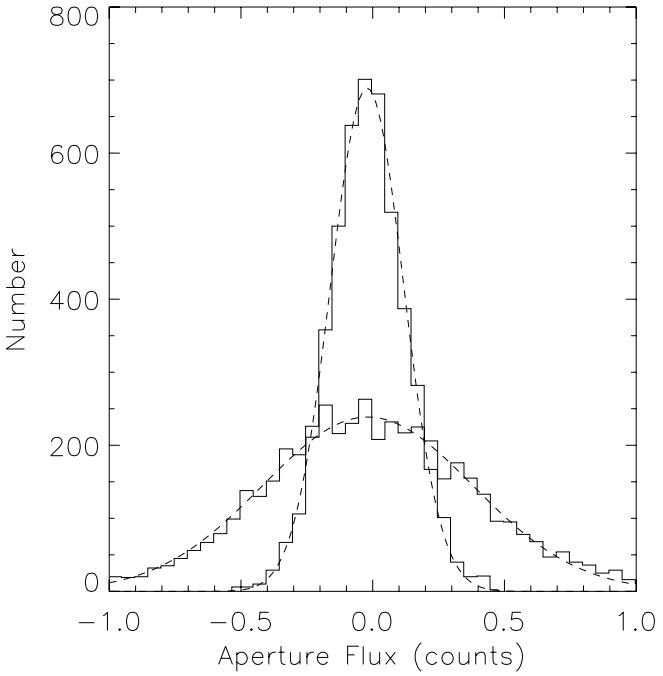

FIG. 2.—Histogram of enclosed fluxes measured on ~5000 empty apertures on the 1030-NE subfield, for two aperture diameters of 0.6″ and 1.1″. Best-fit Gaussians are also shown.

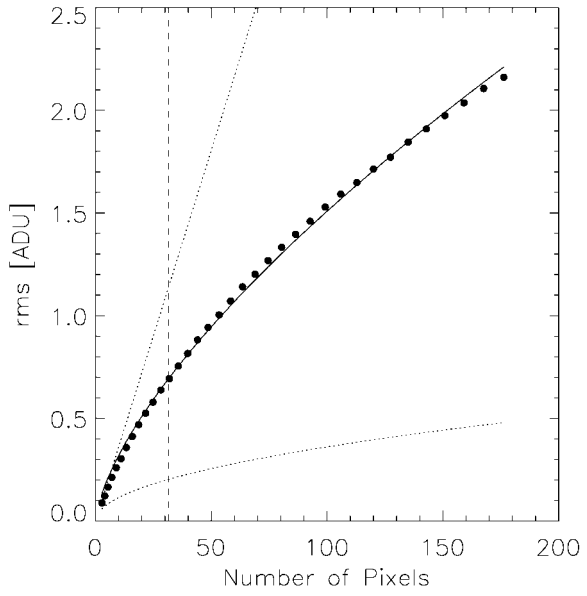

FIG. 3.—Measured background rms (*filled circles*) as a function of the number of pixels in the aperture, and best fit (*solid line*) for the *K*-band mosaic of the 1030 field. The dotted lines show the formal Poisson scaling dependence with $\sigma_n \alpha (n_{\rm pix})^{1/2}$ (*lower line*) and a limiting case with $\sigma_n \alpha n_{\rm pix}$ (*upper line*). The vertical dashed line corresponds to the aperture used for color photometry (see § 5.2).

where σ_1 is the pixel-to-pixel rms, $n_{\rm pix}$ is the number of pixels in the aperture, and α and β are free parameters. In the Poissonian case, we expect $\alpha = 1$ and $\beta = 0.5$. We obtain $\alpha = 1.84$ in both fields, and $\beta = 0.67$ in 1030 and $\beta = 0.71$ in 1255, respectively. Our result is consistent with previous works showing that assuming Poisson noise in the presence of correlated pixels dramatically underestimates photometric uncertainties.

We built an rms map for each *K*-band subfield by taking the inverse square root of the normalized exposure map and scaling it to the rms measured in the $1.4 \times$ FWHM diameter aperture (the choice of this aperture is discussed in § 5.2). We properly combined these maps in order to build a mosaic rms map for the whole field and use it to obtain the photometric uncertainty in a given aperture when performing photometry on our sources.

4.4. *Image Mosaicking*

After the astrometric reprojection of the *K*-band subfields, we obtained images with the same size and physical coordinate system as the MUSYC optical images, so we just needed to combine the images of each subfield in a convenient way in order to create a final *K*-band mosaic of each field. No registration of the frames was necessary. We calculated a weight for each pointing given by

$$w_j = \frac{1}{\left(\text{flux scale}_j \times \text{rms}_j\right)^2}. \quad (11)$$

The difference between this weight and the one used in § 4.1 is that it does not take into account the FWHM, since the subfields have been PSF matched, and the rms is no longer the pixel-to-pixel rms but rather corresponds to the rms of the background in a $1.4 \times$ FWHM diameter aperture estimated as described above. The flux scaling factors correspond to those used to take all the subfields to a common zero point (see § 4.3). The normalized exposure map of each subfield is scaled to the corresponding weight in order to create a final weighting map. Finally, a weighted average of the nine subfield images is taken at every pixel position in order to create the *K*-band mosaic. Figure 4 shows the final *K*-band mosaics of 1030 and 1255.

5. SOURCE DETECTION, PHOTOMETRY, AND *K*-SELECTED CATALOS

5.1. *Detection*

Source detection was performed on the rms-normalized *K*-band mosaic of each field using SExtractor, version 2.5.0 (Bertin & Arnouts 1996). The detection image was built by dividing each *K*-band mosaic by its normalized rms map and then masking the noisy edges of the image (a product of the dithering), as well as the regions around bright saturated stars. After masking, the *K*-band images cover an area of 830 arcmin^2 in 1030, and 828 arcmin^2 in 1255.

In order to find an optimal set of detection parameters (`DETECT_THRSH`, the detection threshold in pixel-to-pixel rms units, and `DETECT_MINAREA`, the number of contiguous pixels that must meet the threshold), we estimated the number of spurious sources in our catalogs by running SExtractor with the same set of parameters on the negative of the detection image, which is a robust estimation, given the Gaussian noise properties of the background. We looked for a set of parameters that maximizes the number of detected sources while keeping the fraction of spurious sources at $K < 20$ under 1%. We found that filtering the images with a PSF-sized kernel lowered the number of detected sources (keeping our spurious fraction constrained), so we did not apply any kind of filtering during the detection. The optimal detection parameters found were `DETECT_MINAREA` = 1 and `DETECT_THRSH` = 3.8 (3.6) for 1030 (1255).

5.2. *Photometry and Color Estimation*

Figure 5 shows the normalized S/N as a function of aperture size for a pointlike source in the 1030 field. Following Gawiser

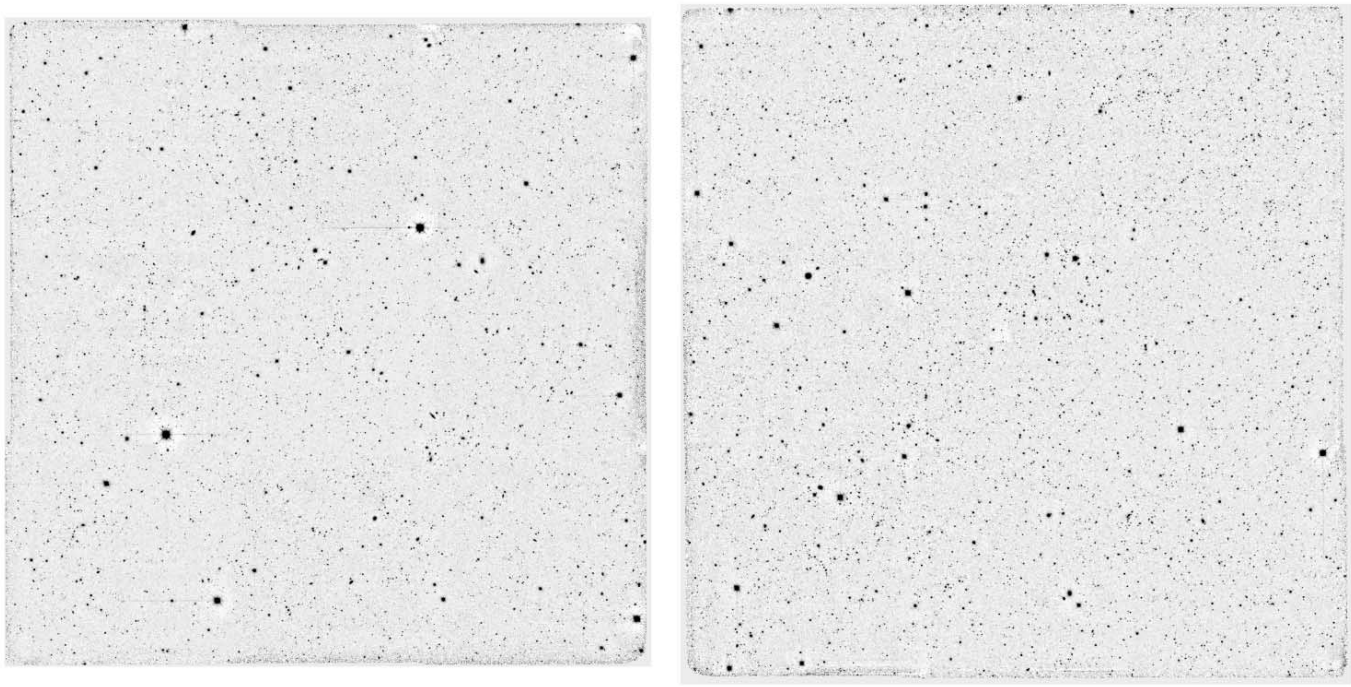

FIG. 4.—Final K-band $\sim 30' \times 30'$ mosaics of the 1030 (*left*) and 1255 (*right*) fields.

et al. (2006a), the S/N is built using the growth curve of the Moffat profile to which the PSF was matched and the noise dependence on aperture size [$\sigma_n(n_{\rm pix})$]. For 1030 and 1255, the S/N is maximized by an aperture of $\sim 1.1 \times$ FWHM. The choice of the aperture used to calculate the colors of our sources is a delicate issue.

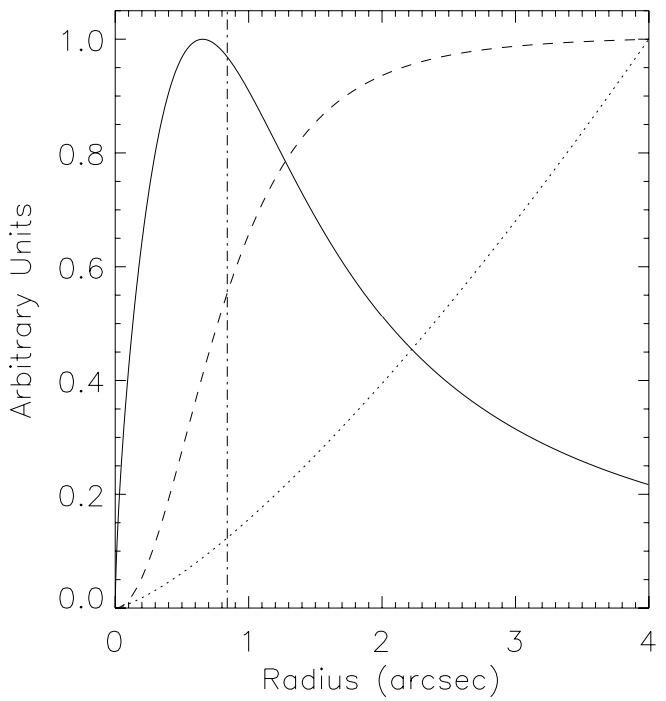

FIG. 5.—S/N for a pointlike source as a function of aperture size for the 1030 field (*solid line*). The dashed curve corresponds to the enclosed flux at a given radius for the field PSF (after PSF matching). The dotted line shows the noise as a function of aperture size presented in Fig. 3. The vertical dash-dotted line marks the radius of the $1.4 \times$ FWHM color aperture used for the photometry.

Choosing a small aperture of $1.1 \times$ FWHM maximizes the S/N but makes the photometry highly dependent on the errors in the PSF matching and the astrometric reprojection of the K-band images. We decided to take a more conservative approach and use a "color aperture" of $1.4 \times$ FWHM (given by the half-light radius of the PSF), for which the S/N is still above 95% of its maximum.

We performed photometry using SExtractor in dual-image mode. In this mode, the detection is performed in the K-band detection image, and photometric measurements are obtained on the images in all bands. We measured the total K-band flux of our sources using a Kron autoscaling elliptical aperture (SExtractor's `FLUX_AUTO`). It has been shown that Kron apertures miss a small fraction (<10%) of the total flux of extended objects (Bertin & Arnouts 1996). We accounted for this loss by applying an aperture correction computed using the growth curve of the PSF and correcting by the fraction of the flux falling outside the characteristic radius of the Kron ellipse given by $r_{\rm Kron} = (ab)^{1/2}$ (where a and b are the major and minor semiaxes, respectively). Corrections are smaller than 0.1 mag for $K < 20$ sources.

Finally, colors were estimated using the flux measured in a circular, fixed $1.4 \times$ FWHM diameter "color aperture" in all bands. Colors, together with the total K-band flux, allow the determination of total fluxes in all bands.

5.3. *K-selected Catalogs*

K-band-selected catalogs are publicly available online.[13] All fluxes and uncertainties are given in units of 0.363 μJy, so the zero point for AB magnitudes is 25 mag. Photometric uncertainties given in the catalogs correspond to the background rms in the corresponding aperture ($\sigma_{\rm bkg}$). Total photometric uncertainties should be calculated as

$$\sigma_{\rm phot} = \sqrt{(\sigma_{\rm bkg})^2 + {\rm flux}}. \quad (12)$$

[13] See http://www.astro.yale.edu/musyc/.

Version 1.0 of the catalogs has the following format:

Column (1): SExtractor ID number.
Columns (2–3): x and y centroid (pixels).
Columns (4–5): α and δ (J2000.0, decimal degrees).
Column (6): internal field code: 1=1030, 2=1255.
Columns (7–20): flux density and error in color aperture (*UBVRIzK*).
Columns (21–22): *K*-band aperture-corrected total flux density and error.
Columns (23–29): exposure time weight normalized to maximum for the field (*UBVRIzK*).
Column (30): color aperture diameter (arcsec).
Column (31): AUTO aperture diameter $2(ab)^{1/2}$ (arcsec).
Column (32): semimajor axis of AUTO aperture (pixels).
Column (33): semiminor axis of AUTO aperture (pixels).
Column (34): AUTO aperture position angle (decimal degrees).
Column (35): AUTO aperture correction factor.
Column (36): SExtractor star/galaxy class.
Column (37): object was originally blended with another.
Column (38): object's neighbors may significantly bias AUTO photometry.
Column (39): SExtractor flag for the *K* band.

6. STAR-GALAXY CLASSIFICATION

We separated stars from galaxies in our catalogs using the two-color criteria introduced by Daddi et al. (2004), in which stars populate a region in the $[(B-z)_{\rm AB}$ versus $(z-K)_{\rm AB}]$ plane (hereafter the *BzK* plane) given by $(z-K)_{\rm AB} < 0.3(B-z)_{\rm AB} - 0.5$. This method was calibrated using the spectroscopically complete K20 survey (Cimatti et al. 2002b) and has been shown to be extremely robust, showing a very high efficiency (>90%) at selecting stars and very little contamination (Daddi et al. 2004). Since the *BzK* method was developed by Daddi using a slightly different set of filters than the ones used in this work (the biggest difference is the use of a Bessel *B* band as opposed to the Johnson *B* band used here), we used the $(B-z)$ and $(z-K)$ colors of 35 stars in the K20 GOODS-South field given by Daddi et al. (2004) and compared them to the colors of the same stars obtained from our *B*-, *z*-, and *K*-band photometry in the ECDF-S field (E. Taylor et al. 2008, in preparation). We applied the computed offsets of -0.04 mag in $(z-K)$ and 0.56 mag in $(B-z)$ to our colors before plotting them in the *BzK* diagram.

This method works better on our data than the star-galaxy classification based on the SExtractor `CLASS_STAR` parameter. The lower panel of Figure 6 shows the *BzK* diagram for sources brighter than $K = 20$ in the 1255 field. We overplotted stars of different spectral types (from O5 to M6) taken from Pickles (1998), all of which fall in the selection region. From the lower panel in Figure 6, we can conclude that the `CLASS_STAR` parameter works correctly on our data up to $K \sim 16$. At fainter magnitudes, the method loses its ability to separate stars from galaxies.

After star-galaxy separation, we detected 1344 stars and 8015 galaxies in 1030, and 1547 stars and 8115 galaxies in 1255 to a magnitude limit of $K = 20$. The number of stars detected is in rough agreement with models of stellar population synthesis in the Milky Way (Robin et al. 2003), which predict a number of $\sim$1100 stars brighter than $K = 20$ for the areas and Galactic coordinates of our fields.

7. NUMBER COUNTS

We computed differential *K*-band number counts in 0.5 mag bins for all galaxies in both fields separately. The results are presented in Figure 7 together with data from the UKIRT Infrared Deep Sky Survey (UKIDSS) Ultra-Deep Survey Early Data Release (UDS EDR) from Lane et al. (2007), the Deep3a-F field from Kong et al. (2006), and the MUSYC Deep NIR Survey (Quadri et al. 2007b). Error bars assume Poisson statistics and underestimate the real errors because cosmic variance is not taken into account. The 1030 and 1255 fields show an excellent agreement (within 1 σ) in their number counts in the $16 \leq K \leq 20$ range. We do not observe the excess in the galaxy number counts observed by Quadri et al. (2007b) in the 1030 field, showing how larger areas (the MUSYC Wide fields are 9 times larger than the MUSYC Deep fields) help to overcome the problem of cosmic variance. We do, however, observe an excess of passive galaxies at $z \sim 2$ in this field, as reported in § 9.1. The flux distribution of galaxies in our sample shows an excellent agreement with previous works. From comparison with the UKIDDS UDS and the MUSYC Deep NIR Survey, both of which are $\sim$1 mag deeper than our survey, we conclude that our sample of *K*-selected galaxies is $\sim$80% complete in the faintest magnitude bin ($19.5 < K < 20$).

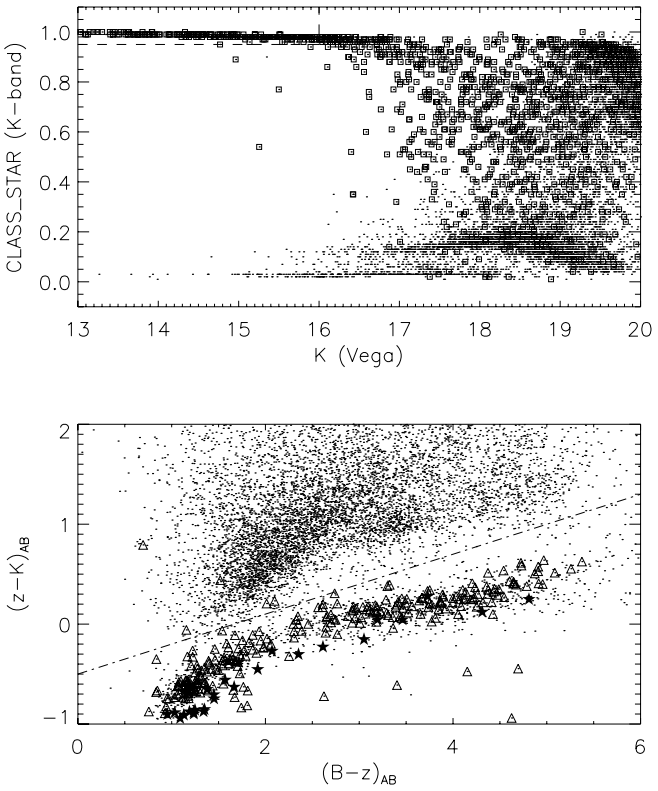

FIG. 6.—*Top*: *K*-band magnitude vs. SExtractor's `CLASS_STAR` parameter for sources brighter than $K = 20$ (*dots*) in the 1255 field. Objects with `CLASS_STAR` ~ 1 are supposed to be pointlike. The dashed lines show the $K < 16$ and `CLASS_STAR` > 0.95 region where the separation works well. Squares correspond to objects classified as stars using the $(z-K)_{\rm AB} < 0.3(B-z)_{\rm AB} - 0.5$ criteria. *Bottom*: *BzK* diagram for sources brighter than $K = 20$ (*dots*) in the same field. Triangles show sources with $K < 16$ and `CLASS_STAR` > 0.95. Stars correspond to stars of different spectral types from Pickles (1998). The dash-dotted line shows the $(z-K)_{\rm AB} = 0.3(B-z)_{\rm AB} - 0.5$ criteria used to separate stars from galaxies.

8. THE *BzK* SELECTION TECHNIQUE

Daddi et al. (2004) introduced two-color selection criteria based on *B*-, *z*-, and *K*-band photometry to select star-forming and passively evolving galaxies in the $1.4 \leq z \leq 2.5$ range. This method is known as the *BzK* selection technique and presents a series of advantages, such as its being almost unbiased against

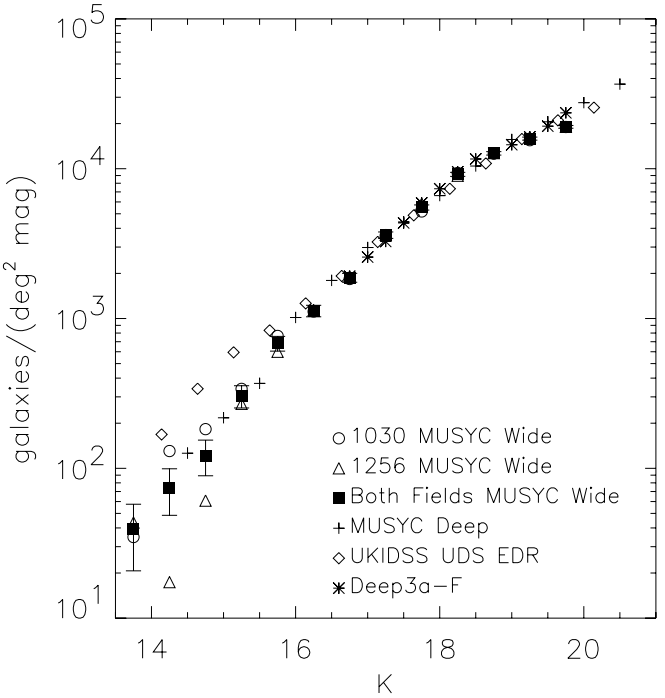

FIG. 7.—Differential K-band number counts for galaxies in 1030 and 1255, together with data from previous works by Kong et al. (2006), Quadri et al. (2007b), and Lane et al. (2007).

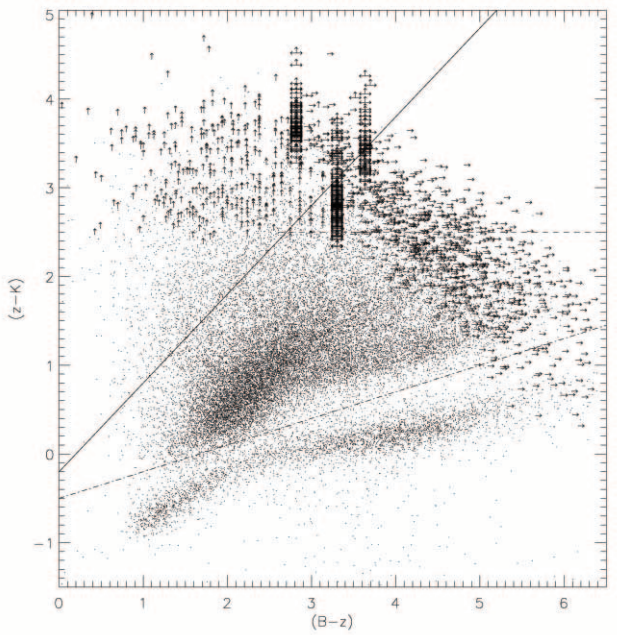

FIG. 8.—*BzK* plane. Dots show the corrected colors of all $K < 20$ sources in the three fields of the MUSYC Wide NIR Survey. The diagonal solid line delimits the *sBzK* selection region ($BzK \geq -0.2$). The horizontal dashed line defines the *pBzK* selection region [$(z-K)_{\rm AB} > 2.5$]. The diagonal dash-dotted line shows the star-galaxy separation criterion [$(z-K)_{\rm AB} < 0.3(B-z)_{\rm AB} - 0.5$].

highly reddened galaxies and its being able to separate star-forming from passive galaxies. Daddi used the 94% spectroscopically complete sample of 311 $K < 20$ galaxies from the K20 survey, which covered 32 arcmin^2 in the GOODS-South field (Cimatti et al. 2002b), to calibrate the method. Star-forming galaxies at $z > 1.4$ (*sBzK*) occupy a well defined region in the *BzK* plane to the left of the solid line shown in Figure 8 and defined by $BzK \equiv (z-K)_{\rm AB} - (B-z)_{\rm AB} \geq -0.2$. Old and passively evolving galaxies at $z > 1.4$ (*pBzK*) are located in the upper right corner of the *BzK* plane, to the right of the solid line and above the dashed line in Figure 8, in a region defined by $BzK < -0.2 \cap (z-K)_{\rm AB} > 2.5$. As stated in § 6, stars are clearly separated from galaxies (especially from those with $z > 1.4$) and are confined to the region under the dash-dotted line in Figure 8, defined by $(z-K)_{\rm AB} < 0.3(B-z)_{\rm AB} - 0.5$. Daddi showed that the method is highly efficient at selecting $z \sim 2$ galaxies and that it presents little contamination from low-z interlopers. The reddening vector in the *BzK* plane is approximately parallel to the *sBzK* selection criteria, which ensures that the method is not biased against heavily reddened dusty galaxies.

9. RESULTS

9.1. *BzK Galaxies in the MUSYC Wide NIR Survey*

We have used our data in the 1030 and 1255 fields together with the MUSYC Wide data in the ECDF-S to select *BzK* galaxies over a total area of 0.71 deg^2 to a limiting depth of $K < 20$. A K-band-selected catalog was produced for the ECDF-S using very similar techniques to the ones used here, and will be presented by E. Taylor et al. (2008, in preparation). By combining the three MUSYC Wide NIR Survey fields, this is the largest area ever surveyed for *BzK* galaxies. Since Daddi et al. (2004) used a slightly different set of filters than the ones used here, we found the need to apply a correction to our color photometry in order to be able to use the *BzK* selection criteria consistently. We have used the $(B-z)$ and $(z-K)$ colors of stars in the K20/GOODS field (which is completely covered by our ECDF-S imaging) provided by Daddi et al. (2004) to compute offsets that we then applied to our measured colors. After correcting our photometry, we applied the *BzK* criteria to our data to produce a large sample of $z \sim 2$ star-forming and passive galaxies.

Figure 8 presents the positions of all $K < 20$ sources in the MUSYC Wide NIR Survey in the *BzK* plane. There are 291 objects that show no detections to the 1 σ level in the B and z bands, appearing as lower limits in $(z-K)$ and having an undetermined $(B-z)$ color in Figure 8. They correspond to 1.0% of the detected sources. This fraction agrees with our expected 1% of spurious sources (see § 5.1), so we assume that most of these objects correspond to spurious detections and eliminate them from our analysis. Galaxies falling in the *sBzK* region and showing lower limits in $(B-z)$, as well as those falling in the *pBzK* region with lower limits in $(z-K)$, cannot be unambiguously classified. There are 73 of these unclassified objects, and for simplicity we leave them outside any further analysis. Including these objects does not affect any of the following results in a significant manner. Out of the 24,399 detected galaxies, we have unambiguously selected a sample of 3261 *BzK* galaxies (2502 *sBzK* and 759 *pBzK*) at $z \sim 2$. This is the largest existing sample of *BzK* galaxies to this depth.

Over the whole surveyed area, *sBzK* galaxies have a sky density of 0.98 ± 0.06 arcmin^{-2}, where we have used the relative deviation between our fields to include cosmic variance when estimating the error. This value is lower than the previous value of 1.2 ± 0.05 arcmin^{-2} obtained by Kong et al. (2006) and consistent with the 0.94 ± 0.17 arcmin^{-2} value for the K20/GOODS sample (Daddi et al. 2004), both values showing only Poisson errors. For *pBzK* galaxies, we obtain a sky density of 0.3 ± 0.1 arcmin^{-2} (again including cosmic variance in the error), consistent with the values obtained by Kong (0.38 ± 0.03 arcmin^{-2}) and Daddi (0.22 ± 0.08 arcmin^{-2}). Due to the considerably larger area surveyed in this work compared to these previous studies and

TABLE 4
Number of Objects and Sky Densities per Field

Field	Galaxies	*sBzK*	*sBzK*[a] (arcmin^{-2})	*pBzK*	*pBzK*[a] (arcmin^{-2})
1030.....	8015	758	0.92 ± 0.03	441	0.50 ± 0.02
1255.....	8115	911	1.10 ± 0.04	165	0.20 ± 0.02
ECDF-S.....	8269	833	0.93 ± 0.03	153	0.17 ± 0.01
Total	24399	2502	0.98 ± 0.06	759	0.30 ± 0.10

[a] Errors for individual fields correspond to Poisson errors. For the total survey, we have included cosmic variance in the error estimation.

the fact that both *sBzK* and *pBzK* galaxies are strongly clustered as we show below, our values for the sky density of these objects are much less affected by cosmic variance and are therefore more representative of the true sky density of these objects.

Table 4 shows the number of *sBzK* and *pBzK* galaxies in our sample and their sky densities for each of our three fields. The GOODS-S field seems to be underdense in DRGs at $z > 2.5$ (Marchesini et al. 2007) and in optically bright AGNs at high redshifts (Dwelly & Page 2006). Furthermore, van Dokkum et al. (2006) found that the sky density of massive ($M > 10^{11}\ M_{\odot}$) *K*-selected galaxies at $2 < z < 3$ in the GOODS-S field is a factor of 3 lower than that of the $10' \times 10'$ MUSYC Deep 1030 field (the densest field in that work). Here, we find a similar trend for passive galaxies in the $1.4 < z < 2.5$ range, where the sky density of *pBzK* galaxies in the $30' \times 30'$ ECDF-S is a factor of 3 lower than in the $30' \times 30'$ 1030. The density of passive $z \sim 2$ galaxies in the ECDF-S field is 60% of the mean value for the whole survey, while in the 1030 field it is a factor of 1.7 higher. Interestingly, star-forming galaxies at $z \sim 2$ show no sign of a significant underdensity.

The large number of objects in our sample allows us to clearly identify the new branch of galaxies in the *BzK* diagram reported by Lane et al. (2007). This feature runs parallel to the stellar sequence in the $2.5 < (B - z) < 5.0$ range at $(z - K) \sim 1.0$. Lane found it to be consistent with the track of passively evolving early-type galaxies at $z < 1.4$. This is the first confirmation of the existence of this new branch since it was reported.

9.2. *Redshift Distribution*

Photometric redshifts rely on the presence of continuum spectral features in the galaxy SED that are strong enough to show up in broadband photometry. The most prominent features of this kind are the Lyman break at 912 Å and the 4000 Å break. At $z \sim 1.5$, the 4000 Å break is just redward of the *z* band, and the Lyman break is ~1000 Å blueward from the *U* band. As we move to higher redshifts, no strong spectral features are sampled by our broadband photometry (*UBVRIzK*) until we reach $z \sim 2.6$, where the Lyman break enters the *U* band (the 4000 Å break is not sampled by the *K* band until $z \sim 4$). This means that using our data alone, we are unable to estimate reliable photometric redshifts for our sample of *BzK* galaxies, since they inhabit a nearly identical redshift range to that in which we cannot sample any spectral continuum features. We would not have this problem if we had *J*- and *H*-band imaging of our fields.

To overcome this problem, we used the data from the MUSYC Deep NIR Survey, which cover a smaller area to a greater depth and include *JHK* near-infrared imaging, as well as the *UBVRIz* optical coverage. All the data in the Deep Survey were taken using the same instrument as the data presented here, and were reduced using analogous techniques. We have limited the Deep Survey catalog to $K < 20$ and used the same color corrections and selection criteria explained above to select a sample of 514 *BzK* galaxies (365 *sBzK* and 149 *pBzK*). This sample should be representative of our *BzK* galaxy sample, since there are no significant differences in the selection biases involved.

Photometric redshifts of the Deep Survey galaxies were calculated with the methods described by Rudnick et al. (2001) using linear combinations of four Coleman et al. (1980) empirical templates, two starburst templates from Kinney et al. (1996), and two solar metallicity, dust-free 10 Myr and 1 Gyr old single stellar population templates (Bruzual & Charlot 2003). For more details on the photo-*z* estimations, see Quadri et al. (2007b).

Figure 9 shows the redshift distribution $N(z)$ of $K < 20$ *pBzK* and *sBzK* galaxies in the Deep Survey. Both distributions are fairly Gaussian and cover the expected redshift range for *BzK* galaxies, roughly $1.4 \lesssim z \lesssim 2.5$. The distribution of *sBzK* galaxies is clearly broader than the distribution for *pBzK*. The peak at the $1.25 < z < 1.5$ bin in the *pBzK* distribution comes from the 1030 field and is not present in any of the other three Deep Survey fields. As can be seen from Table 4, the 1030 wide field shows an excess of *pBzK* galaxies of a factor of 1.7 with respect to the whole survey. This overdensity, together with the presence of the peak in the redshift distribution, might indicate the presence of a large-scale structure at $z \sim 1.4$ in the 1030 field.

Like Hayashi et al. (2007), we obtain best Gaussian fits of our redshift distributions, but in our case we correct them for the effects introduced by the large errors involved in photometric redshift estimations as explained below and use these to recover the correlation length from the angular correlation function through the inverse Limber projection (see § 9.5). In that work, Hayashi used the spectroscopic redshift distribution of bright ($K < 20.1$) *sBzK* galaxies to compute correlation lengths (r_0) for a much deeper sample of *sBzK* ($K < 21.3$) galaxies, under the assumption that $N(z)$ is not dependent on *K* magnitude. This latter assumption was proven to be wrong by Quadri et al. (2007b) using the MUSYC Deep NIR Survey data. By looking at Figure 12 of Quadri et al. (2007b), it is clear that the redshift distribution of *sBzK* galaxies is severely broadened when going to fainter magnitudes ($K < 21$), as the *BzK* technique loses its power to select galaxies in a well-determined and narrow redshift range. This broadening of $N(z)$ for $K > 20$ *BzK* galaxies was also reported by Reddy et al. (2005) using spectroscopic redshifts of *sBzK* galaxies in the GOODS-N field. Assuming a much narrower redshift distribution during the clustering analysis should underestimate the real value of r_0, and this might affect the level of clustering measured by Hayashi et al. (2007) in their faint sample of *sBzK* galaxies.

The observed $N(z)$ is strongly affected by errors in the photometric redshifts. In the redshift range of interest, the Deep Survey photometric redshifts show a dispersion of $\Delta z/(1 + z) = 0.12$ when compared to spectroscopic redshifts drawn from the literature (Quadri et al. 2007a). To a first approximation, under the basic assumption that $N(z)$ is a normal distribution and that photometric redshift errors are of a Gaussian nature, the net effect of the errors is to broaden the intrinsic redshift distribution. The observed distribution in this case is the result of the convolution of the intrinsic distribution and the photometric error distribution. This is a delicate issue because of the assumptions involved in this argument. First, we are assuming that the scatter in the photometric redshift is not redshift dependent, which, given the narrow range over which *BzK* galaxies are selected, seems like a reasonable approximation. Also, uncertainties in photometric redshifts are subject to a series of systematics related to the methods used to estimate them (templates used, photometric errors in different bands, aliasing of SED features, etc.), which can lead to

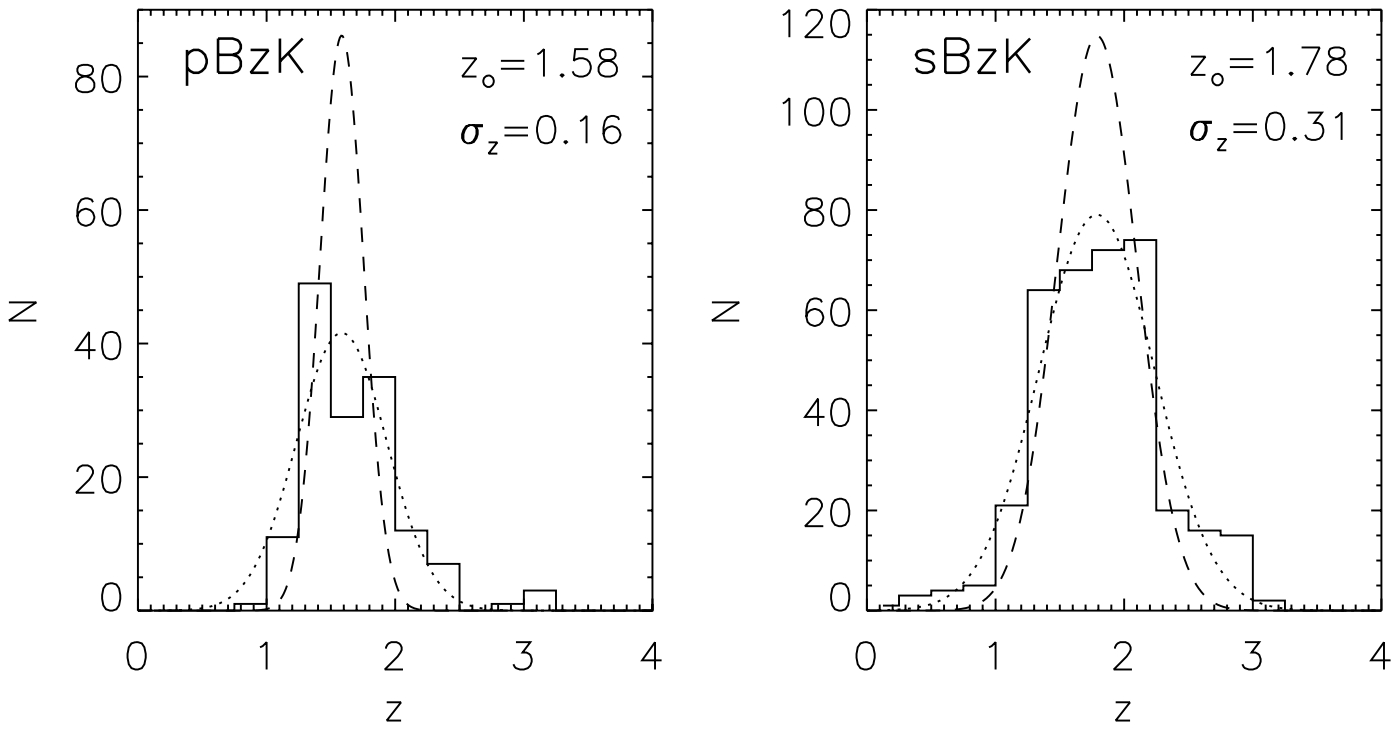

FIG. 9.—Photometric redshift distribution of $K < 20$ *pBzK* and *sBzK* galaxies in the MUSYC Deep NIR Survey. Dotted lines correspond to the best Gaussian fit to the observed redshift distribution $N_{\rm obs}(z)$. Dashed lines correspond to the distribution after correcting for the broadening due to errors in the photometric redshifts. The parameters reported correspond to the corrected distribution $N_{\rm corr}(z)$.

a non-Gaussian distribution of errors. Nonetheless, unless a very specific and unlikely combination of error distribution and redshift dependence of this distribution occurs, the net effect of photometric uncertainties is to broaden the intrinsic redshift distribution considerably, and this effect must be taken into account in order to avoid significant overestimation of the level of clustering of the galaxies in the sample.

The best Gaussian fits to the observed $N(z)$ are centered at $z_0 = 1.58 \pm 0.04$ and $z_0 = 1.78 \pm 0.03$, and have a width of $\sigma_{z,\rm obs} = 0.35 \pm 0.04$ and $\sigma_{z,\rm obs} = 0.45 \pm 0.03$ for *pBzK* and *sBzK* galaxies, respectively; they are shown as the dotted lines in Figure 9. Errors in the parameters come from Monte Carlo simulations of 1000 renditions of $N(z)$, where the redshifts of the galaxies were varied within their uncertainties. We have deconvolved these from our assumed Gaussian distribution of photometric errors of width Δz, as determined by Quadri et al. (2007a) and measured at the center of the distribution for each population, to obtain our estimates of the intrinsic redshift distribution $N_{\rm corr}(z)$. The intrinsic distributions are shown as dashed lines in Figure 9, normalized to the total number of objects in each sample, and have widths of $\sigma_z = 0.17 \pm 0.06$ and $\sigma_z = 0.31 \pm 0.04$ for *pBzK* and *sBzK* galaxies, respectively. The latter value is comfortingly consistent with the 0.35 obtained by Hayashi et al. (2007) for a sample of 81 *sBzK* galaxies with spectroscopic redshifts, which supports the validity of the above assumptions.

9.3. *Stellar Masses, Reddening, and Star Formation Rates*

Besides calibrating the *BzK* method, Daddi et al. (2004) used Bruzual & Charlot (2003) models to perform SED fitting of the K20/GOODS galaxies with known spectroscopic redshifts to calibrate relations that estimate the stellar mass of *BzK* galaxies and the reddening of *sBzK* galaxies based on the *B*-, *z*-, and *K*-band photometry alone. Daddi also gave a recipe to estimate the ongoing star formation rate (SFR) of *sBzK* galaxies using the *B* flux (rest-frame UV flux) based on calibrations by Madau et al. (1998). For details on the calibration of these methods and the uncertainties involved in them, see Daddi et al. (2004). We have used these relations to calculate stellar masses, reddening [$E(B-V)$], and SFRs of the galaxies in our sample. It is worth noting that, since we do not have redshift information for individual galaxies, these results should be interpreted in a statistical sense, especially the SFR estimates. Daddi et al. (2004) showed that mass estimates have uncertainties of $\sim$60% for single objects, and $E(B-V)$ estimates show a residual rms of about 0.06 when compared to the values obtained from the multiband SED fitting of objects with known spectroscopic redshifts. In any case, given the large number of galaxies in our sample and the narrow Gaussian shape of the redshift distributions presented in the previous section, the median stellar masses, $E(B-V)$, and SFRs should be highly representative of the properties of typical *BzK* galaxies at $z \sim 2$.

The top panel in Figure 10 shows the distribution of stellar masses of *sBzK* and *pBzK* galaxies in our sample. It can be seen that *sBzK* galaxies span a broader range in mass than *pBzK* galaxies, extending down to masses of a few $10^{10}\ M_\odot$, while the lowest mass *pBzK* galaxies in our sample have $\sim 10^{11}\ M_\odot$. The median mass of *sBzK* galaxies is $\sim 1.0 \times 10^{11}\ M_\odot$, while *pBzK* galaxies have a median mass of $\sim 1.6 \times 10^{11}\ M_\odot$. These results are in excellent agreement with the results of Kong et al. (2006) in the Deep3a-F. As noted in that work, the lower limit of the mass distribution of *pBzK* galaxies corresponds to the mass of a $K = 20$ galaxy lying on top of the $(z-K) = 2.5$ selection limit, and hence has its origin in the construction of the *pBzK* sample.

The $E(B-V)$ distribution for *sBzK* galaxies is shown in the central panel of Figure 10. Daddi's recipe for estimating reddening uses the $(B-z)$ color as a measure of the UV slope of the

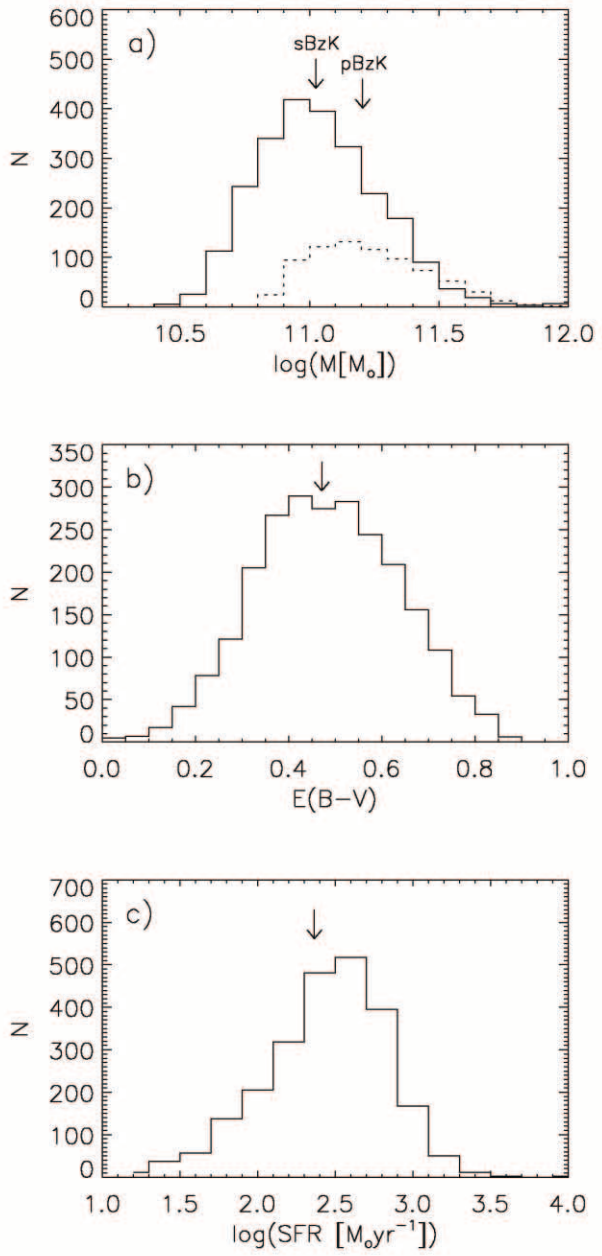

FIG. 10.—(*a*) Distribution of stellar masses of *sBzK* (*solid line*) and *pBzK* (*dotted line*) galaxies. (*b*) Histogram of $E(B-V)$ values for star-forming *BzK* galaxies in the sample. (*c*) Histogram of SFR calculated using the dereddened *B*-band flux of *sBzK* galaxies. Arrows indicate median values of the distributions.

SED and assumes a gray and self-similar Calzetti et al. (2000) extinction law. The median reddening of our *sBzK* galaxies is $E(B-V)=0.47$. Adelberger & Steidel (2000) present the distribution of extinction at 1600 Å for Lyman break galaxies at $z\sim3$. Under the Calzetti extinction law assumption, it can be seen that practically no galaxies with $E(B-V)>0.45$ are selected by the LBG technique. Reddy et al. (2005) show that for spectroscopically confirmed BM/BX galaxies at $z>1$, typical $E(B-V)$ values are lower than 0.3. This means that at least 55% of the *sBzK* galaxies in our sample would not be detected by rest-frame UV-continuum-based selection techniques.

SFRs of *sBzK* galaxies were estimated using the *B*-band flux as the 1500 Å rest-frame flux (the *B*-band effective wavelength corresponds to 1845 Å at $z=1.4$, 1593 Å at $z=1.78$, and 1265 Å at $z=2.5$) and the calibration by Madau et al. (1998). UV fluxes were dereddened using the estimated $E(B-V)$ values for each galaxy. As stated above, the lack of knowledge of the distance modulus of our galaxies means that these SFR estimates are not reliable for individual objects, but the median SFR of the sample should correspond to the typical SFR of *sBzK* galaxies. The distribution of SFRs is presented in the bottom panel of Figure 10, and it shows a median value of $\simeq230\ M_\odot\ \mathrm{yr}^{-1}$. This value is similar to, but slightly higher than, previous estimates by Daddi et al. (2004) and Kong et al. (2006). Given our survey comoving volume of 8.7×10^6 Mpc^3 (roughly $1.4<z<2.5$), we compute a number density of *sBzK* galaxies of $\sim3\times10^{-4}$ Mpc^{-3}, which translates to a star formation rate density (SFRD) of $\sim0.07\ M_\odot\ \mathrm{yr}^{-1}\ \mathrm{Mpc}^{-3}$. The latest estimates of the SFRD at $z\sim2$, based on rest-frame UV-selected samples (Reddy et al. 2008), show a SFRD $\simeq 0.2\ M_\odot\ \mathrm{yr}^{-1}\ \mathrm{Mpc}^{-3}$ at $z=2$. NIR-bright *sBzK* galaxies can account for about 30% of this total SFRD. Considering that UV selection methods miss approximately half of *sBzK* galaxies, the inclusion of bright ($K<20$) star-forming *BzK* galaxies in the SFRD would increase its value by approximately 15%.

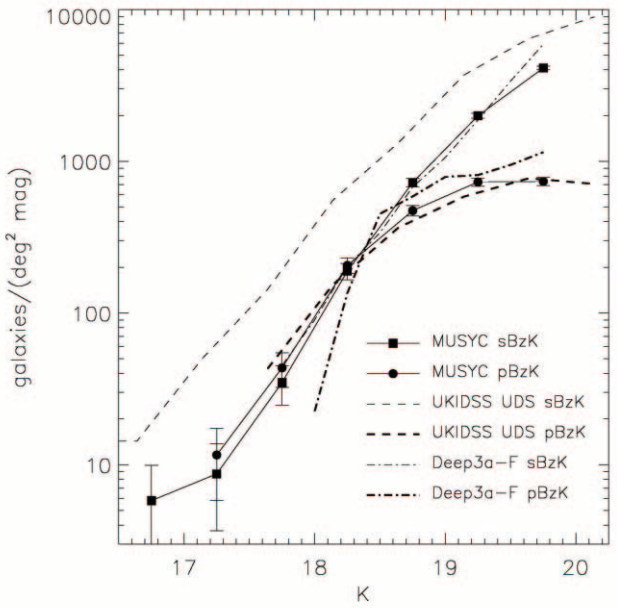

FIG. 11.—Differential *K*-band number counts of $K<20$ *sBzK* (*squares*) and *pBzK* (*circles*) galaxies in the MUSYC Wide NIR Survey, together with data from previous works by Kong et al. (2006) and Lane et al. (2007).

9.4. *Number Counts of BzK Galaxies*

In Figure 11 and Table 5, we present differential *K*-band number counts for *sBzK* and *pBzK* galaxies in our sample, together

TABLE 5
MUSYC *BzK* GALAXIES DIFFERENTIAL NUMBER COUNTS

K bin center (mag)	*sBzK* [$\log(N\ \mathrm{deg}^{-2}\ \mathrm{mag}^{-1})$]	*pBzK* [$\log(N\ \mathrm{deg}^{-2}\ \mathrm{mag}^{-1})$]
16.75.....	0.763	...
17.25.....	0.939	1.064
17.75.....	1.541	1.638
18.25.....	2.275	2.313
18.75.....	2.860	2.674
19.25.....	3.300	2.864
19.75.....	3.615	2.867

with previous estimates by Kong et al. (2006) and Lane et al. (2007). The number counts of *sBzK* galaxies are very steep, and the number of objects increases sharply toward higher magnitudes. On the other hand, passive *BzK* galaxies exhibit a flattening in the number counts toward fainter magnitudes, with a knee around $K \sim 18.5$. This behavior has been observed in previous works and is attributed to the fact that because of the narrow redshift distribution of *pBzK* galaxies, the number counts actually probe the luminosity function of these objects. Star-forming *BzK* galaxies do not show this behavior. This has usually been attributed to the fact that *sBzK* galaxies have a wider redshift distribution than *pBzK* galaxies (Kong et al. 2006; Lane et al. 2007). Although *sBzK* galaxies have a wider redshift distribution than *pBzK* galaxies in our sample, this difference in the number counts might just as easily be related to intrinsic differences between the luminosity function of both populations. Marchesini et al. (2007) showed that the faint-end slope of the luminosity function of galaxies with blue rest-frame UV color in the $2 < z < 2.5$ range is much steeper than for galaxies showing a redder rest-frame UV color. A qualitative comparison of Figure 11 and Figure 5 in Marchesini et al. (2007) supports this statement. Further study is necessary to decouple the effects of these differences in the redshift distribution and the luminosity function on the shape of the number counts.

Number counts of *pBzK* galaxies show an excellent agreement with previous results by Lane et al. (2007) on the UKIDSS UDS field, and a somewhat worse agreement with the Kong et al. (2006) sample that can be attributed to the small number of objects in the Deep3a-F, especially at bright magnitudes. On the other hand, number counts of *sBzK* galaxies in our sample are in perfect agreement with the *sBzK* sample in the Deep3a-F (a factor of $\sim$3 more numerous than the *pBzK* sample in the same field). Both Kong's number counts and the ones presented here are systematically lower than the number counts of *sBzK* galaxies in the UKIDSS UDS sample over the whole magnitude range. The origin of this discrepancy lies in the fact that in this work, as well as in Kong's, *BzK* colors were corrected in order to take into account the difference between the filters used and those used by Daddi et al. (2004) to calibrate the *BzK* method. Lane et al. (2007) did not apply this correction, and hence their *BzK* selection criteria were not used in a manner consistent with the original calibration of the method. Not applying this correction caused an effective offset of $\sim$0.5 mag toward lower values in the $(B - z)$ colors of their objects [or equivalently an offset of the selection criteria limit toward higher values of $(B - z)$]. As can clearly be seen by inspecting Figure 8, this offset produces a significant excess of objects selected as *sBzK* galaxies but does not affect the *pBzK* sample in such a radical manner (which explains our agreement with Lane's *pBzK* number counts). This excess of low-z contaminants in the UKIDSS UDS *sBzK* sample can account for the discrepancy observed in the number counts.

9.5. *Clustering of BzK Galaxies*

9.5.1. *The Angular Two-Point Correlation Function*

The angular two-point correlation function $\omega(\theta)$ is a useful statistic that helps us to characterize the clustering properties of galaxies on the sky plane, in terms of the joint probability $\delta P = N^2[1 + \omega(\theta)]\delta\Omega_1\delta\Omega_2$ of finding two galaxies in the infinitesimal solid angles $\delta\Omega_1$ and $\delta\Omega_2$ separated by an angular distance θ and given a surface density of objects N, with respect to what is expected for a Poissonian random distribution (Peebles 1980).

Usually, $\omega(\theta)$ is estimated by comparing the count of galaxy pairs with angular separation θ found in the observed field to the number of similar pairs obtained from a catalog of random and independently distributed objects. Several estimators have been designed to quantify this statistic, and in this work we use the estimator proposed by Landy & Szalay (1993), which has the advantage of being unbiased and of showing nearly Poisson variance:

$$\hat{\omega}(\theta) = \left[\frac{DR(\theta)}{n_{dd}} - \frac{2DR(\theta)}{n_{dr}} + \frac{RR(\theta)}{n_{rr}}\right] \Big/ \frac{RR(\theta)}{n_{rr}}. \quad (13)$$

Here, $DD(\theta)$ is the observed number of galaxy pairs with separations in the interval $[\theta, \theta + \delta\theta]$, $RR(\theta)$ is the analogous number obtained from a random catalog that completely imitates the field angular geometry, and $DR(\theta)$ is the amount of observed-random cross pairs with separations in the cited range. Each of these quantities is normalized by the total number of pairs in the sample, which correspond, respectively, to $n_{dd} = N_d(N_d - 1)/2$, $n_{rr} = N_r(N_r - 1)/2$, and $n_{dr} = N_r N_d$, where N_d and N_r represent the total number of objects in the observed and random catalogs, respectively.

We calculated $\hat{\omega}(\theta)$ in angular distance bins of constant logarithmic width $\Delta \log \theta = 0.15$. In order to produce random samples that replicate the survey geometry, we constructed angular masks over the K-band images used for galaxy detection, tracing the field borders and leaving out regions occupied by bright foreground stars or any image artifacts that prohibit source detection. We then generated catalogs of 1000 random points located inside the angular mask and calculated $\hat{\omega}(\theta)$ repeatedly over 25 different catalogs in order to obtain a total random sample $\sim$100 times larger than the observed one. We counted random, observed, and crossed pairs in each field separately, and then combined the resulting $DD(\theta)$, $RR(\theta)$, and $DR(\theta)$ for each bin to produce the angular correlation function for all *sBzK* and *pBzK* galaxies found in the three fields of the MUSYC Wide NIR Survey. Since our three fields have practically identical areas and depths, the number of galaxies in each field is dominated by large-scale structure rather than observational limits. Because of this, we have taken the approach of calculating a single correlation function for the whole survey by counting all pairs in the three fields instead of computing a single $\omega(\theta)$ for each field and averaging the results. We consider our approach to be more statistically robust, since a low number of objects in an angular bin can translate into very noisy estimations. A full derivation of this approach of handling multiple fields to calculate $\omega(\theta)$ is given by Francke et al. (2008). The uncertainty in $\hat{\omega}(\theta)$ was estimated using a jackknife method in which we divided each field into 25 smaller regions and repeated the estimations of $\hat{\omega}(\theta)$, eliminating one subarea at a time. In this way, the standard deviation for each angular distance bin was obtained. For a detailed study on the robustness of the jackknife method, see the Appendix in Zehavi et al. (2002).

The angular correlation function is typically modeled by a power law of the form $\omega(\theta) = A_\omega\theta^{1-\gamma}$. The limited size of our sample does not allow an independent and significant measure of both the amplitude and the slope of $\omega(\theta)$, so in the rest of the analysis we assume a value of $\gamma = 1.8$, which is consistent with slopes measured in faint- and bright-galaxy surveys (Zehavi et al. 2002). This also allows a direct comparison with previous work (Kong et al. 2006; Hayashi et al. 2007). Since we are estimating $\omega(\theta)$ in a finite region of the sky, we are affected by an uncertainty in the estimation of the background galaxy surface density (Peebles 1980; Infante 1994) that is corrected by introducing a

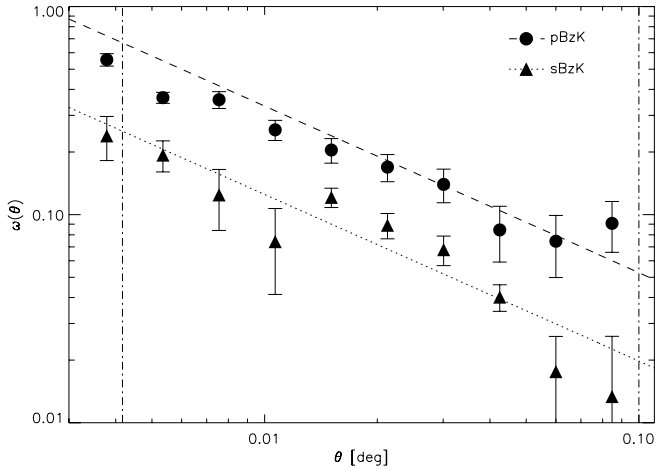

FIG. 12.—Measured angular correlation functions of *sBzK* (*triangles*) and *pBzK* (*circles*) galaxies in the MUSYC Wide NIR Survey. Best power-law fits for *sBzK* (*dotted line*) and *pBzK* (*dashed line*) galaxies are also shown. The vertical dot-dashed lines correspond to the $15'' < \theta < 0.1^\circ$ range used for the fitting.

negative offset, so that a more accurate parameterization of $\omega(\theta)$ is given by

$$\omega(\theta) = A_\omega(\theta^{1-\gamma} - C). \quad (14)$$

This bias is known as the "integral constraint," and, as shown by Roche et al. (1999), can be estimated numerically by

$$C = \frac{\sum RR(\theta)\theta^{1-\gamma}}{\sum RR(\theta)}, \quad (15)$$

which renders a value of $C = 1.89$. Once we have applied this correction, we fit the amplitude through minimization of χ^2. For fitting purposes, we only consider separations in the $15'' < \theta < 0.1^\circ$ range. The lower limit corresponds to half a virial radius (r_{200}) of a halo of $\sim 10^{13}\ M_\odot$ at $z = 2$, in order to avoid the contribution of the "one-halo" term (i.e., a clustering signal coming from galaxies that share DM halos). We experimented by setting larger lower limits for the bins to be considered for the fit (up to $\theta > 40''$) and observed variations in the final values of the correlation lengths r_0 on the order of 0.1 σ; therefore, we are confident that our results have not been affected by effects introduced by galaxies inhabiting the same halos. The upper limit is taken in order to avoid spurious signals coming from border effects.

The measured two-point angular correlation functions of passive and star-forming *BzK* galaxies in the MUSYC Wide NIR sample, together with the best-fitting power laws, are shown in Figure 12. It is clear that there is a positive correlation signal for both *sBzK* and *pBzK* galaxies, and that passive *BzK* galaxies are more strongly clustered than star-forming *BzK* galaxies at $z \sim 2$. Most points in the correlation function of both *sBzK* and *pBzK* galaxies are consistent with a pure power-law fit within the 2 σ uncertainties, and all of them are consistent to a 3 σ level. Therefore, we have not found any significant evidence of structure in $\omega(\theta)$ for either of the two populations.

Table 6 reports the best-fitting values for the amplitudes of $\omega(\theta)$. For *sBzK* galaxies we obtain $A_\omega = (3.14 \pm 1.12) \times 10^{-3}$, and for *pBzK* galaxies we get $A_\omega = (8.35 \pm 1.55) \times 10^{-3}$. These values are systematically lower but still in statistical agreement with the only previous estimate of the correlation function of bright $K < 20$ *BzK* galaxies by Kong et al. (2006), who obtained values of $A_\omega = (4.95 \pm 1.69) \times 10^{-3}$ and $A_\omega = (10.40 \pm 2.83) \times 10^{-3}$ for *sBzK* and *pBzK* galaxies, respectively, in the Deep3a-F field. The systematically lower amplitudes of the correlation functions, together with the surface densities (see § 9.1) measured for both *sBzK* and *pBzK* galaxies, which are lower in this work than in Kong et al. (2006), indicate that the Deep3a-F field, which is 8 times smaller than the area covered in this work, shows a level of clustering above the cosmic average, demonstrating once again the importance of large-area surveys in overcoming cosmic variance.

9.5.2. *Correlation Lengths, Bias, and Dark Matter Halo Masses*

Under the assumption of a power-law form for $\omega(\theta)$, the two-point spatial correlation function $\xi(r)$ also corresponds to a power law with index $-\gamma$. Usually, $\xi(r)$ is parameterized in terms of the correlation length r_0 and the slope γ as

$$\xi(r) = \left(\frac{r}{r_0}\right)^{-\gamma}. \quad (16)$$

The parameter r_0 can be calculated from the angular correlation function using the inverse Limber transformation (Limber 1953; Peebles 1980), which leads to the relation expressed by Kovač et al. (2007):

$$A_\omega = r_0^\gamma \sqrt{\pi} \frac{\Gamma[(\gamma-1)/2]}{\Gamma(\gamma/2)} \times \frac{\int_0^\infty F(z) D_A^{1-\gamma}(z) N_{\rm corr}(z)^2 g(z)\, dz}{\left[\int_0^\infty N_{\rm corr}(z)\, dz\right]^2}, \quad (17)$$

where A_ω is the amplitude of $\omega(\theta)$, $D_A(z)$ is the angular diameter distance, $g(z)$ is a cosmology-dependent expression given by

$$g(z) = \frac{H_0}{c}(1+z)^2 \sqrt{1 + \Omega_M z + \Omega_\Lambda \left[(1+z)^{-2} - 1\right]}, \quad (18)$$

and $F(z)$ accounts for the redshift evolution of $\xi(r)$ described by $F(z) = (1+z)^{-(3+\epsilon)}$, where $\epsilon = -1.2$ if the clustering is fixed in

TABLE 6
CLUSTERING PROPERTIES OF MUSYC *BzK* GALAXIES

Population	$N_{\rm gal}$	A_ω[a] (10^{-3})	z_0[b]	σ_z[b]	r_0 (h_{70}^{-1} Mpc)	σ_{r_0,σ_z}[c]	σ_{r_0,A_ω}[d]	Bias	$M_{\rm DH}^{\rm min}$ ($M_\odot$)
pBzK	759	8.35 ± 1.55	1.58	0.16 ± 0.04	10.82 ± 1.72	1.35	1.07	$3.27^{+0.46}_{-0.47}$	1×10^{13}
sBzK	2502	3.14 ± 1.12	1.78	0.31 ± 0.06	8.89 ± 2.03	1.00	1.77	$2.93^{+0.59}_{-0.60}$	4×10^{12}

[a] Amplitude of the angular correlation function with slope parameter $\gamma = 1.8$.
[b] Parameters of Gaussian fit to the redshift distribution $N_{\rm corr}(z)$.
[c] Dispersion in r_0 due to photometric redshift errors.
[d] Dispersion in r_0 due to uncertainty in A_ω.

comoving coordinates, $\epsilon = 0$ if the clustering is fixed in proper coordinates, or $\epsilon = 0.8$ according to the prediction of linear theory (Brainerd et al. 1995). In this work, we assume the first case of constant clustering in comoving coordinates. Finally, $N_{\rm corr}(z)$ corresponds to the redshift distribution of the studied population, which we have modeled as Gaussian distributions with the parameters reported in Table 6 (see § 2).

We considered two sources of error in our r_0 calculations: (1) the uncertainty in the measurement of A_ω (σ_{r_0, A_ω}) and (2) the uncertainty in the photometric redshifts used to construct the redshift distribution of both *sBzK* and *pBzK* galaxies (σ_{r_0, σ_z}). We estimated these two errors separately and added them in quadrature to obtain the uncertainty in the reported r_0 values. In the first case, we used a Monte Carlo approach, varying the A_ω values within their measured uncertainties using a normal distribution of errors, and then computed the dispersion of the resultant r_0 values calculated using a fixed $N_{\rm corr}(z)$ with the parameters reported in Table 6. In order to estimate the errors coming from the uncertainty in the redshift distribution, we followed the approach of Hayashi et al. (2007), who showed that the Limber transformation is insensitive to changes in z_0, when the width σ_z of the redshift distribution is the dominant source of uncertainty. As above, we have estimated the uncertainty coming from σ_z by varying it within its error (assumed Gaussian), but keeping A_ω fixed. Table 6 independently reports both uncertainties for the two populations, together with the measured correlation lengths.

For *sBzK* galaxies, we measured $r_0 = 8.89 \pm 2.03$ Mpc, a value that is much lower than, although barely consistent to a 1 σ level with, the $r_0 = 12.14^{+2.9}_{-3.3}$ Mpc ($8.5^{+2.0}_{-2.3}\ h_{100}^{-1}$ Mpc) measured by Hayashi et al. (2007) for $K < 20$ *sBzK* galaxies in the Deep3a-F sample by Kong et al. (2006). This is in agreement with the above evidence showing that the Deep3a-F field is denser and more clustered than the median field. We also measured $r_0 = 10.82 \pm 1.72$ Mpc for *pBzK* galaxies. This is the first measurement of the correlation length of passive *BzK* galaxies ever reported.

In the context of the ΛCDM scenario, galaxies form by the cooling and condensation of baryonic gas in the cores of dark matter halos. The galaxy spatial correlation function is then associated with the auto-correlation function of DM halos, and the spatial distribution of galaxies of a certain type is biased in the same way as that of their hosting halos with respect to the underlying mass distribution (Mo & White 1996). In the context of the ellipsoidal collapse model extension of the Press-Schechter formalism by Sheth et al. (2001), they are related to a first approximation by the linear bias. Following the methods of Quadri et al. (2007a) and Francke et al. (2008), we estimated the galaxy effective bias adopting the following definition:

$$b_{\rm eff}^2 = \frac{\sigma_{8,\,\rm gal}^2}{\sigma_{8,\,\rm DM}^2(z)}, \tag{19}$$

where σ_8^2 corresponds to the variance (of galaxies or dark matter) in 8 h_{100}^{-1} Mpc radius spheres. We then estimated the minimum mass $M_{\rm DH}^{\rm min}$ of DM halos hosting galaxies in our sample, given by

$$b_{\rm eff} = \frac{\int_{M_{\rm DH}^{\rm min}}^{\infty} b(M_{\rm DH}) n(M_{\rm DH})\, dM_{\rm DH}}{\int_{M_{\rm DH}^{\rm min}}^{\infty} n(M_{\rm DH})\, dM_{\rm DH}}, \tag{20}$$

where $b(M_{\rm DH})$ is the bias parameter for halos of mass $M_{\rm DH}$ taken from Sheth et al. (2001), and $n(M_{\rm DH})dM_{\rm DH}$ is the halo mass function derived by Sheth & Tormen (1999). We assumed the simplest case of one galaxy per halo. All the above expressions were evaluated at the center of the redshift distribution for each of the two populations studied, that is, $z_0 = 1.58$ for *pBzK* galaxies, and $z_0 = 1.78$ for *sBzK* galaxies, and obtained values of $b_{\rm eff} = 2.93^{+0.59}_{-0.60}$ for star-forming *BzK* galaxies, which corresponds to a minimum halo mass of $M_{\rm DH}^{\rm min} = 4 \times 10^{12}\ M_\odot$, and $b_{\rm eff} = 3.27^{+0.46}_{-0.47}$ for passive *BzK* galaxies, which corresponds to $M_{\rm DH}^{\rm min} = 9 \times 10^{12}\ M_\odot$.

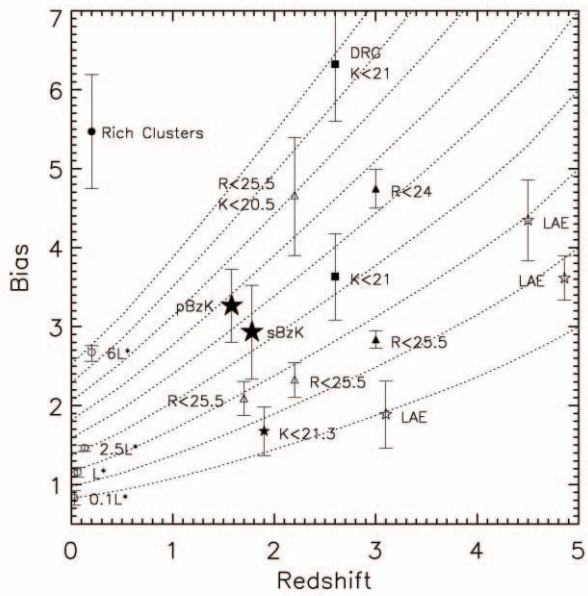

FIG. 13.—Tracks of bias redshift evolution calculated using the "halo merging" model. Large filled stars show the bias of the $K < 20$ *sBzK* and *pBzK* galaxies calculated in this work. Also presented are the biases of faint *sBzK* galaxies from Hayashi et al. (2007; *small filled stars*); BM/BX galaxies with $\mathcal{R} < 25.2$ and $K < 20.5$ BX galaxies (*open triangles)* from Adelberger et al. (2005b) and Adelberger et al. (2005a), respectively; LBGs at $z \sim 3$ from Lee et al. (2006; *filled triangles*); $K < 21$ DRGs and *K*-selected galaxies at $2.0 < z < 3.5$ from Quadri et al. (2007a; *squares*); LAEs at $z = 3.1$, $z = 4.5$, and $z = 4.86$ (*open stars*) from Gawiser et al. (2007), Kovač et al. (2007), and Ouchi et al. (2003), respectively; local SDSS galaxies from Zehavi et al. (2005; *open circles*); and rich clusters from Bahcall et al. (2003; *filled circle*).

By comparing the biases of different populations of galaxies at different redshifts, we can obtain insights into the evolution of these systems. Figure 13 shows tracks for the evolution of the bias with redshift together with measured bias factor values for different populations drawn from the literature. Previous work by Quadri et al. (2007a) and Gawiser et al. (2007) have presented similar plots using the "no-merging" model of Fry (1996). As dark matter becomes more clustered with time, the bias factor of a biased population decreases. It is important to note that we expect mergers to play a more important role in higher density regions than in less dense regions, where galaxies have a lower probability of merging. Hence, including the effects of merging would translate into a steeper evolution of the bias with redshift. Therefore, the tracks calculated using the "no-merging" model only provide an upper limit for the bias factor of a given point at lower redshifts. In this work, we present bias evolution tracks obtained from the "halo merging model" (Bond et al. 1991; Bower 1991; Lacey & Cole 1993), in which at any given redshift halos have a defined probability of merging into higher mass halos, so that there is a defined mass distribution of descendant halos. For a given halo mass (bias) at a given redshift, the tracks follow the bias of the most likely descendant halo population, that is, the mode of the conditional mass distribution function evaluated at lower redshifts.

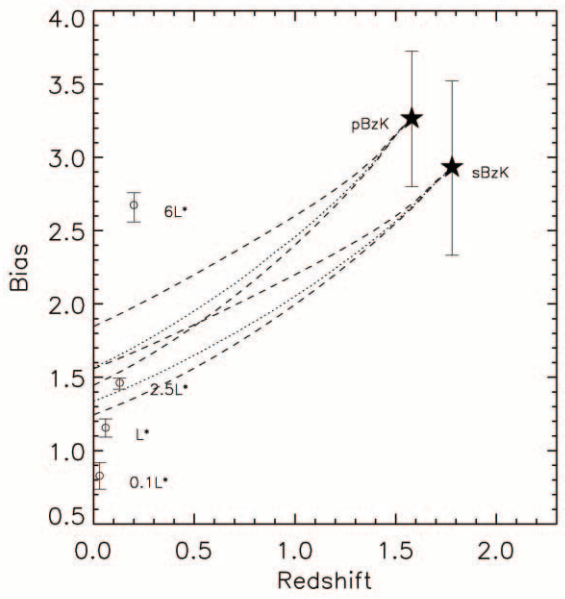

FIG. 14.—Tracks of bias redshift evolution of $K < 20$ *pBzK* and *sBzK* galaxies. Dotted lines show the bias of the most likely descendant halo population. Dashed lines mark the bias of halos whose likelihood is reduced by a factor $\exp(-1/2)$ with respect to the maximum likelihood; in the case of a Gaussian distribution of descendants, this would correspond to $\pm 1\ \sigma$. The probability distribution of descendant halo masses is clearly nonsymmetrical.

It can be seen that although passive *BzK* galaxies in our sample show a higher bias than star-forming *BzK* galaxies, their clustering level is still consistent, and both populations inhabit halos in similar mass ranges. Both *sBzK* and *pBzK* galaxies are consistent with being descendants of the bright LBG population at $z \sim 3$. Bright LBGs have typical stellar masses of $\sim 10^{10}$–$10^{11}\ M_{\odot}$ (Papovich et al. 2001; Iwata et al. 2005); therefore, given the $\sim$2 Gyr time between $z = 3$ and $z = 1.6$, they could easily assemble enough mass to reach the typical masses of *BzK* galaxies, given a reasonable SFR of 10–100 $M_{\odot}\ \mathrm{yr}^{-1}$. High-redshift LAE populations are not consistent with being the progenitors of *BzK* galaxies. It can also be seen that *K*-bright UV-selected galaxies at $z \sim 2$ (the $K < 20.5$ BX population) are more clustered than *BzK* galaxies, although the BX sample clustering measurement could suffer from cosmic variance (Adelberger et al. 2005a). In any case, the trend is consistent with what is observed at fainter magnitude limits, where faint *sBzK* galaxies show a lower clustering level than the BM/BX sample. On the other hand, as can be seen in Figure 14, the NIR-bright *BzK* galaxies presented in this work are consistent with being the predecessors of massive early-type $>1L_{*}$ galaxies in the local universe, usually present in groups and clusters, but are totally inconsistent with being associated with the progenitors of the central galaxies of rich clusters. The most likely descendants of *K*-bright *sBzK* and *pBzK* galaxies have bias factors of $1.3^{+0.2}_{-0.1}$ and $1.6^{+0.3}_{-0.1}$ at $z = 0$.

10. SUMMARY AND CONCLUSIONS

In this paper, we have presented *K*-band imaging of two of the three $30' \times 30'$ fields that comprise the MUSYC Wide NIR Survey. We have given details of our data reduction procedures, as well as our source detection algorithms. By combining our data with the MUSYC *UBVRIz* optical imaging, we have constructed *K*-band-selected source catalogs that reach a 5 σ point-source limiting depth of $K = 20$. Catalogs are publicly available as part of the MUSYC Public Data Release and present spatial and photometric information for the 16,130 galaxies and 2891 stars brighter than $K = 20$ detected in the 1030 and 1255 fields. We have also presented *K*-band differential number counts for galaxies in the two fields, which show excellent agreement with previous *K*-selected samples.

By combining our data with the MUSYC *K*-selected catalog of the ECDF-S field, we have selected a sample of 2502 star-forming and 759 passively evolving *BzK* galaxies at $z \sim 2$ over a very large area, allowing us to study the spatial distribution of these galaxies and minimizing the effects of cosmic variance. We reported sky surface densities of $0.98 \pm 0.06\ \mathrm{arcmin}^{-2}$ for *sBzK* galaxies and of 0.30 ± 0.10 for *pBzK* galaxies. The large area surveyed over three noncontiguous fields allows the measurement of realistic uncertainties in the reported densities. We have found that the ECDF-S field is underdense in passive galaxies at $z \sim 2$ when compared to the mean for the complete survey, which is in agreement with previous studies on the density of DRGs and *K*-selected massive galaxies. We have also confirmed the existence of the passively evolving early-type galaxy track at $z < 1.4$ discovered by Lane et al. (2007).

Using the methods calibrated by Daddi et al. (2004), we estimated stellar masses of the *BzK* galaxies in our sample and showed that star-forming *BzK* galaxies have typical masses of $\sim 1.0 \times 10^{11}\ M_{\odot}$, while passive *BzK* objects have $\sim 1.6 \times 10^{11}\ M_{\odot}$. We also estimated the reddening and the SFR in our sample of star-forming *BzK* objects. The *sBzK* galaxies show a median reddening of $E(B - V) = 0.47$, implying that at least 55% of them would be missed by UV-continuum-based selection techniques. This is in excellent agreement with current studies on the overlap of galaxy populations at these redshifts (Reddy et al. 2005; Quadri et al. 2007b; Grazian et al. 2007). Star-forming *BzK* galaxies also showed large median SFRs of $\simeq 230\ M_{\odot}\ \mathrm{yr}^{-1}$, implying that bright $K < 20$ *sBzK* galaxies can account for up to 30% of the SFRD at $z \sim 2$.

We also presented redshift distributions of both *sBzK* and *pBzK* galaxies that show that both populations are selected over a narrow and well-determined redshift range, with the *pBzK* population showing a narrower distribution than that of *sBzK* galaxies. We corrected these distributions to take into account the broadening introduced by errors in the photometric redshift estimation, and used them to deproject the angular correlation function of the two populations.

The two-point angular correlation functions for *pBzK* and *sBzK* galaxies were presented, together with their best fits. We used the corrected redshift distributions to deproject the spatial correlation function from the angular one and estimated correlation lengths r_0 of 8.89 ± 2.03 Mpc and 10.82 ± 1.72 Mpc for *sBzK* and *pBzK* galaxies, respectively, which translate into bias factor values of $2.93^{+0.59}_{-0.60}$ and $3.27^{+0.46}_{-0.47}$, respectively. By comparing the effective bias of the spatial distribution of the two populations with that of DM halos, we estimated minimum halo masses of $4 \times 10^{12}\ M_{\odot}$ and $9 \times 10^{12}\ M_{\odot}$ for *sBzK* and *pBzK* galaxies, respectively.

Finally, we compared the bias of different populations of galaxies at different redshifts, and concluded that NIR-bright $K < 20$ *sBzK* and *pBzK* galaxies are consistent with being the descendants of bright LBGs at $z \sim 3$, and the progenitors of local galaxies with $\lesssim 1L_{*}$. This corresponds to the bright end of the luminosity function of present-day galaxies. The fact that *K*-bright *BzK* galaxies evolve into very bright and massive systems is not surprising given their high stellar masses and large SFRs at $z \sim 2$. In the future, pushing the limits of *K*-band surveys to fainter magnitudes will allow us to detect large samples of the progenitors of

current $<1L_*$ galaxies through *BzK* selection, overlapping these samples with the LAE population and opening a window to a more complete study of the ancestors of normal galaxies in the local universe.

We acknowledge the valuable support from FONDAP Centro de Astrofísica, FONDECYT projects 1040423 and 1040719, and the Astronomy Departments of the Universidad de Chile and Yale University. We also thank the staff of Cerro Tololo Inter-American Observatory for their invaluable assistance with our observations. This research has made use of NASA's Astrophysics Data System. Finally, we thank the referee for helpful comments, which helped to improve the quality of this work.

Facilities: CTIO(ISPI, MOSAIC II)

REFERENCES

Adelberger, K. L., Erb, D. K., Steidel, C. C., Reddy, N. A., Pettini, M., & Shapley, A. E. 2005a, ApJ, 620, L75
Adelberger, K. L., & Steidel, C. C. 2000, ApJ, 544, 218
Adelberger, K. L., Steidel, C. C., Pettini, M., Shapley, A. E., Reddy, N. A., & Erb, D. K. 2005b, ApJ, 619, 697
Adelberger, K. L., Steidel, C. C., Shapley, A. E., Hunt, M. P., Erb, D. K., Reddy, N. A., & Pettini, M. 2004, ApJ, 607, 226
Bahcall, N. A., Dong, F., Hao, L., Bode, P., Annis, J., Gunn, J. E., & Schneider, D. P. 2003, ApJ, 599, 814
Bertin, E., & Arnouts, S. 1996, A&AS, 117, 393
Bond, J. R., Cole, S., Efstathiou, G., & Kaiser, N. 1991, ApJ, 379, 440
Bower, R. G. 1991, MNRAS, 248, 332
Brainerd, T. G., Smail, I., & Mould, J. 1995, MNRAS, 275, 781
Bruzual, G., & Charlot, S. 2003, MNRAS, 344, 1000
Calzetti, D., Armus, L., Bohlin, R. C., Kinney, A. L., Koornneef, J., & Storchi-Bergmann, T. 2000, ApJ, 533, 682
Chen, H.-W., et al. 2002, ApJ, 570, 54
Cimatti, A., et al. 2002a, A&A, 381, L68
———. 2002b, A&A, 392, 395
Coleman, G. D., Wu, C.-C., & Weedman, D. W. 1980, ApJS, 43, 393
Daddi, E., Cimatti, A., Renzini, A., Fontana, A., Mignoli, M., Pozzetti, L., Tozzi, P., & Zamorani, G. 2004, ApJ, 617, 746
Dwelly, T., & Page, M. J. 2006, MNRAS, 372, 1755
Erb, D. K., Shapley, A. E., Steidel, C. C., Pettini, M., Adelberger, K. L., Hunt, M. P., Moorwood, A. F. M., & Cuby, J.-G. 2003, ApJ, 591, 101
Francke, H., et al. 2008, ApJ, 673, L13
Franx, M., et al. 2003, ApJ, 587, L79
Fry, J. N. 1996, ApJ, 461, L65
Gawiser, E., et al. 2006a, ApJS, 162, 1
———. 2006b, ApJ, 642, L13
———. 2007, ApJ, 671, 278
Grazian, A., et al. 2007, A&A, 465, 393
Gronwall, C., et al. 2007, ApJ, 667, 79
Hayashi, M., Shimasaku, K., Motohara, K., Yoshida, M., Okamura, S., & Kashikawa, N. 2007, ApJ, 660, 72
Hu, E. M., Cowie, L. L., & McMahon, R. G. 1998, ApJ, 502, L99
Infante, L. 1994, A&A, 282, 353
Iwata, I., Inoue, A. K., & Burgarella, D. 2005, A&A, 440, 881
Joyce, R. R. 1992, in ASP Conf. Ser. 23, Astronomical CCD Observing and Reduction Techniques, ed. S. B. Howell (San Francisco: ASP), 258
Kinney, A. L., Calzetti, D., Bohlin, R. C., McQuade, K., Storchi-Bergmann, T., & Schmitt, H. R. 1996, ApJ, 467, 38
Kong, X., et al. 2006, ApJ, 638, 72
Kovač, K., Somerville, R. S., Rhoads, J. E., Malhotra, S., & Wang, J. 2007, ApJ, 668, 15
Labbé, I., et al. 2003, AJ, 125, 1107
Lacey, C., & Cole, S. 1993, MNRAS, 262, 627
Landy, S. D., & Szalay, A. S. 1993, ApJ, 412, 64
Lane, K. P., et al. 2007, MNRAS, 379, L25
Lee, K.-S., Giavalisco, M., Gnedin, O. Y., Somerville, R. S., Ferguson, H. C., Dickinson, M., & Ouchi, M. 2006, ApJ, 642, 63
Limber, D. N. 1953, ApJ, 117, 134
Lucy, L. B. 1974, AJ, 79, 745
Madau, P., Pozzetti, L., & Dickinson, M. 1998, ApJ, 498, 106
Marchesini, D., et al. 2007, ApJ, 656, 42
Mo, H. J., & White, S. D. M. 1996, MNRAS, 282, 347
Ouchi, M., et al. 2003, ApJ, 582, 60
Papovich, C., Dickinson, M., & Ferguson, H. C. 2001, ApJ, 559, 620
Peebles, P. J. E. 1980, The Large-Scale Structure of the Universe (Princeton: Princeton Univ. Press)
Pickles, A. J. 1998, PASP, 110, 863
Quadri, R., et al. 2007a, ApJ, 654, 138
———. 2007b, AJ, 134, 1103
Reddy, N. A., Erb, D. K., Steidel, C. C., Shapley, A. E., Adelberger, K. L., & Pettini, M. 2005, ApJ, 633, 748
Reddy, N. A., Steidel, C. C., Pettini, M., Adelberger, K. L., Shapley, A. E., Erb, D. K., & Dickinson, M. 2008, ApJS, 175, 48
Richardson, W. H. 1972, J. Opt. Soc. Am., 62, 55
Robin, A. C., Reylé, C., Derrière, S., & Picaud, S. 2003, A&A, 409, 523
Roche, N., Eales, S. A., Hippelein, H., & Willott, C. J. 1999, MNRAS, 306, 538
Rudnick, G., et al. 2001, AJ, 122, 2205
Schlegel, D. J., Finkbeiner, D. P., & Davis, M. 1998, ApJ, 500, 525
Sheth, R. K., Mo, H. J., & Tormen, G. 2001, MNRAS, 323, 1
Sheth, R. K., & Tormen, G. 1999, MNRAS, 308, 119
Skrutskie, M. F., et al. 2006, AJ, 131, 1163
Smail, I., Ivison, R., Blain, A., Kneib, J. P., & Owen, F. 2000, in ASP Conf. Ser. 195, Imaging the Universe in Three Dimensions, ed. W. van Breugel & J. Bland-Hawthorn (San Francisco: ASP), 248
Steidel, C. C., Giavalisco, M., Pettini, M., Dickinson, M., & Adelberger, K. L. 1996, ApJ, 462, L17
Thompson, D., et al. 1999, ApJ, 523, 100
van Dokkum, P. G., et al. 2006, ApJ, 638, L59
———. 2003, ApJ, 587, L83
Virani, S. N., Treister, E., Urry, C. M., & Gawiser, E. 2006, AJ, 131, 2373
Zehavi, I., et al. 2002, ApJ, 571, 172
———. 2005, ApJ, 630, 1